



1 **Understanding Aerosol-Cloud Interactions in a Single-Column** 2 **Model: Intercomparison with Process-Level Models and Evaluation** 3 **against ACTIVATE Field Measurements**

4 Shuaiqi Tang¹, Hailong Wang¹, Xiang-Yu Li¹, Jingyi Chen¹, Armin Sorooshian^{2,3}, Xubin Zeng², Ewan
5 Crosbie^{4,5}, Kenneth L. Thornhill⁴, Luke D. Ziemba⁴, Christiane Voigt^{6,7}

6 ¹Atmospheric, Climate, and Earth Science Division, Pacific Northwest National Laboratory, Richland, WA, USA

7 ²Department of Hydrology and Atmospheric Sciences, The University of Arizona, Tucson, AZ, USA

8 ³Department of Chemical and Environmental Engineering, The University of Arizona, Tucson, AZ, USA

9 ⁴NASA Langley Research Center, Hampton, VA, USA

10 ⁵Analytical Mechanics Associates Inc., Hampton, VA, USA

11 ⁶Deutsches Zentrum für Luft- und Raumfahrt, Oberpfaffenhofen, Germany

12 ⁷Johannes Gutenberg-Universität, Mainz, Germany

13 *Correspondence to:* Shuaiqi Tang (shuaiqi.tang@pnnl.gov) and Hailong Wang (hailong.wang@pnnl.gov)

14 **Abstract.** Marine boundary-layer clouds play a critical role in the Earth's energy balance. Their microphysical and radiative
15 properties are highly impacted by ambient aerosols and dynamical forcings. In this study, we evaluate the representation of
16 these clouds and related aerosol-cloud interactions processes in the single-column version of E3SM climate model (SCM),
17 against field measurements collected during the NASA ACTIVATE campaign over the western North Atlantic, as well as
18 intercompare with high-resolution process-level models. Results show that E3SM-SCM, driven by the ERA5 reanalysis,
19 reproduces the cloud properties as good as the high-resolution WRF simulations. For stronger surface forcings combined
20 with a weaker subsidence taken from a WRF cloud-resolving simulation, both E3SM-SCM and WRF large-eddy simulation
21 produce thicker clouds. This indicates that a proper combination of large-scale dynamics, sub-grid scale parameterizations,
22 and model configurations is needed to obtain optimal performance of cloud simulations. In the E3SM-SCM sensitivity tests
23 with fixed dynamics but perturbed aerosol properties, higher aerosol number concentration leads to more numerous but
24 smaller cloud droplets, resulting in a stronger shortwave cloud forcing (i.e., stronger radiative cooling). This apparent
25 Twomey effect is consistent with prior climate model studies. Cloud liquid water path shows a weakly positive relation with
26 cloud droplet number concentration associated with precipitation suppression, which is different from the nonlinear relation
27 approximated from prior observations and E3SM studies, warranting future investigation. Our findings indicate that the
28 SCM framework is a key tool to bridge the gap between climate models, high-resolution models, and field observations to
29 facilitate process-level understanding.



30 **1 Introduction**

31 Marine boundary layer (MBL) clouds are the dominant cloud type over oceans, with an annual mean occurrence frequency
32 of 45% (Warren et al., 1988) and coverage of 34% including stratocumulus, stratus and fog (Warren et al., 1988) or 23% for
33 stratocumulus only (Wood, 2012). Its high reflectivity overlapped with low-reflective ocean surface underneath leads to a
34 strong shortwave cooling effect, but its longwave warming effect is neglectable due to low cloud top height (Hartmann et al.,
35 1992). In global climate models (GCM), the representation of MBL clouds and their radiative effects has long been a
36 challenging task (e.g., Bony and Dufresne, 2005; Brunke et al., 2019). Even the latest Coupled Model Intercomparison
37 Project Phase 6 (CMIP6) models still have a large inter-model spread in the cloud shortwave effect (Bock et al., 2020) that
38 introduces large uncertainties to climate projection.

39
40 The western North Atlantic Ocean (WNAO) is one of the regions dominated by MBL clouds. The Gulf Stream with large
41 spatial gradient in sea surface temperature (SST), strong synoptical systems such as tropical and extratropical cyclones,
42 aerosols generated locally or transported from the adjacent North American continent, all contribute to the complex aerosol-
43 cloud-meteorology-ocean interactions over this region (e.g., Painemal et al., 2021; Corral et al., 2021). Recently, Sorooshian
44 et al. (2020) provided an overview of the past atmospheric studies over WNAO region, followed by more detailed overviews
45 on circulation, boundary layer and clouds (Painemal et al., 2021), clouds and precipitation (Kirschler et al., 2023), and
46 atmospheric chemistry and aerosols (Corral et al., 2021). However, among 715 peer-reviewed publications between 1946
47 and 2019, only 2% of the studies are related to aerosol-cloud interactions (ACI) (Sorooshian et al., 2020). This indicates that
48 ACI over WNAO region is underexplored, considering that ACI has long been emphasized as the largest uncertainty source
49 in climate model simulations (IPCC, 2013, 2021).

50
51 With the limited prior understanding, a three-year field campaign, Aerosol Cloud meTeorology Interactions oVer the
52 western ATlantic Experiment (ACTIVATE) project (Sorooshian et al., 2019), was conducted between 2020 and 2022
53 targeting the complex ACI for MBL clouds over the WNAO region. Two aircraft flew simultaneously in spatial
54 coordination: a low-flying aircraft making in-situ measurements and a high-flying aircraft making remote-sensing
55 measurements and releasing dropsondes. Among the total of 162 flights, 12 of them were conducted as “process study”
56 flights (Sorooshian et al., 2023), during which the flying patterns of the two flights were carefully designed to provide
57 detailed information about the scene encompassing the clouds of interest. In some cases, including the case chosen for this
58 study, the high-flying aircraft released numerous dropsondes along a large circle and the low-flying aircraft conducted
59 stacked below-, in-, and above-cloud flight legs within the circle. The dropsonde-derived divergence profiles and surface
60 fluxes have been used to constrain process-level modelling studies (Chen et al., 2022; Li et al., 2022; Li et al., 2023).

61



62 A few process-level studies have been conducted using the Weather Research and Forecasting (WRF) model nested domain
63 regional simulation (Chen et al., 2022) and WRF large-eddy simulation (LES) (Li et al., 2022; Li et al., 2023). The WRF
64 regional simulation has an inner domain at 1 km convection-permitting horizontal grid spacing, hereafter referred to as
65 cloud-resolving model (CRM) simulation in this study. Note that this is different from the conventionally defined CRM,
66 which is usually run with prescribed large-scale forcing, periodic boundary conditions, in a limited region analogous to a
67 single-column model (SCM) (Randall et al., 1996). A post-frontal MBL cloud case related to a winter cold-air outbreak
68 (CAO) was studied in these CRM and LES studies. Chen et al. (2022) successfully simulated the observed cloud roll
69 structure in WRF-CRM. They found that a distinctive boundary layer wind direction shear favours the formation and
70 persistence of cloud rolls. Li et al. (2022) validated the ERA5-derived large-scale forcing with dropsonde-derived forcing
71 and tested the sensitivity of WRF-LES to the large-scale forcing. They furthermore investigated ACI with a series of LES
72 sensitivity experiments based on spatial variability in aircraft-measured aerosol and cloud properties (Li et al., 2023).

73

74 In this study, we focus on SCM simulations for the same CAO case investigated in Chen et al. (2022); Li et al. (2022); Li et
75 al. (2023). As these models simulate the same case in different complexity and resolution, we are now able to make detailed
76 process-level analysis of ACI through the multi-scale LES-CRM-SCM intercomparison. This is a step further than studies
77 using individual model. Our first goal is to understand how the CAO-related post-frontal MBL clouds are simulated in the
78 SCM in contrast to the LES and CRM simulations, and the observations. Another goal is to explore how the simulated MBL
79 clouds respond to perturbations of aerosol properties prescribed into the SCM through sensitivity studies using observations
80 collected during the ACTIVATE campaign. We introduce the selected case, data, and models in Sect. 2, intercompare SCM
81 with CRM and LES results in Sect. 3, and then show results of SCM sensitivity studies in Sect. 4. Conclusion remarks are
82 provided in Sect. 5.

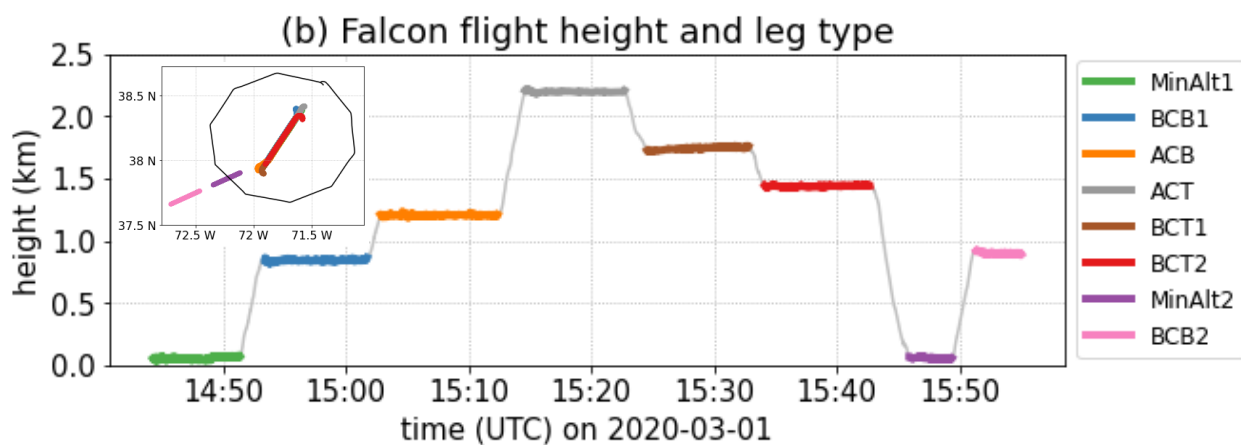
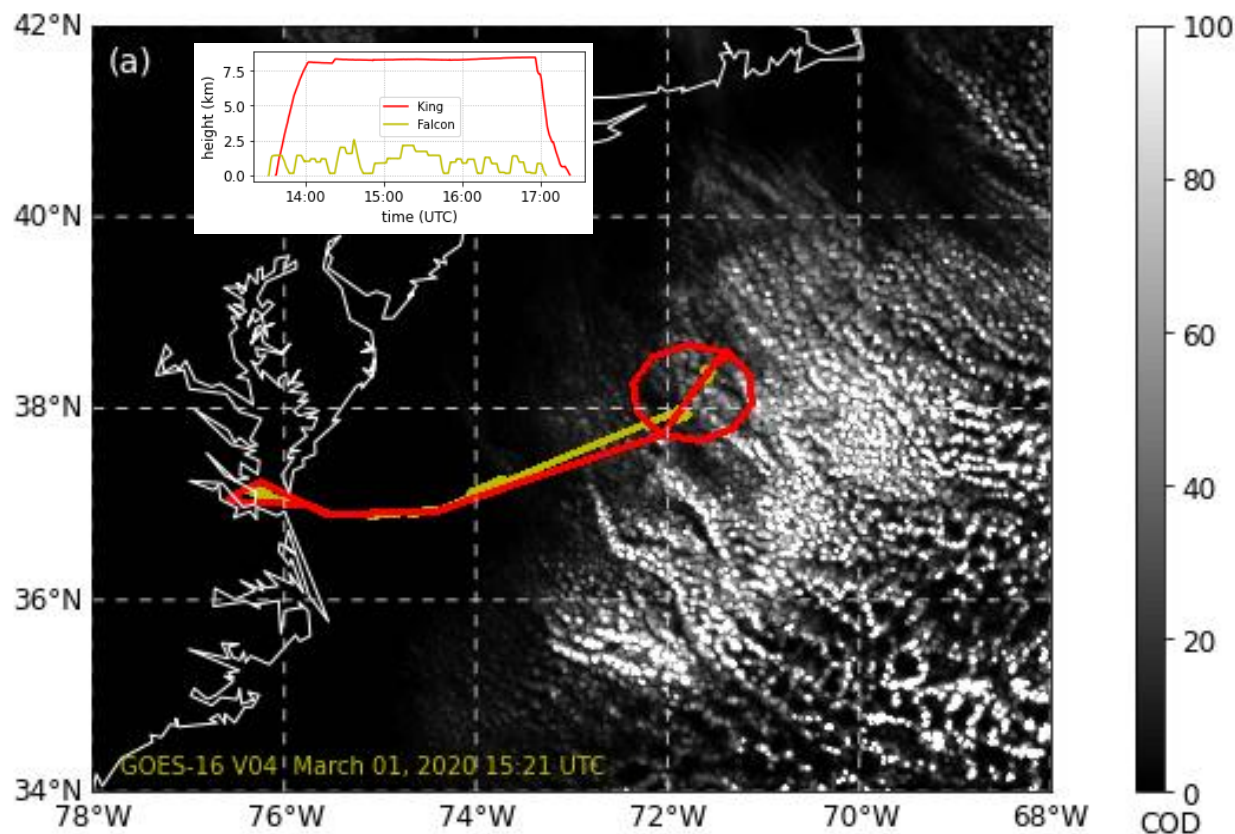
83 **2 Case Description, Observations and Simulations**

84 **2.1 The CAO case on 1 March 2020**

85 This study focuses on a CAO case observed on 1 March 2020, after the passage of a cold front. A large area of MBL clouds
86 formed associated with warm SST, cold air advection, and large-scale subsidence. The ACTIVATE campaign deployed two
87 spatially coordinated aircraft to measure the post-frontal MBL clouds from different heights (Fig. 1a). The High Spectral
88 Resolution Lidar – generation 2 (HSRL-2) from the high-flying King Air aircraft measured vertical aerosol backscattering
89 profiles, which were used to estimate the cloud top height. The King Air also released 11 dropsondes in a ~110 km diameter
90 circle centered near (38.1°N, 71.7°W) to measure the vertical profiles of the meteorology state. The low-flying Falcon
91 aircraft mainly provided in-situ aerosol and cloud microphysical measurements. The entire Falcon flight is divided into many
92 flight “legs” (Dadashazar et al., 2022b). Each flight leg represents a segment during which the flight is measuring under a
93 specific condition at constant altitude (e.g., below/in/above cloud) or is in a specific operation mode (e.g., ascending,



94 descending). For most of this study, we focus on eight flight legs within or near the dropsonde array domain (Fig. 1b),
 95 including two minimum-altitude (MinAlt) legs, two below-cloud-base (BCB) legs, one above-cloud-base (ACB) leg, two
 96 below-cloud-top (BCT) legs, and one above-cloud-top (ACT) leg. The first six flight legs were stacked in different heights as
 97 a “wall” pattern. The last two legs were flying outside the dropsonde domain but used here for sensitivity study purpose.



98



99 **Figure 1: (a). ACTIVATE flight tracks for Falcon (yellow) and King Air (red) aircraft on 1 March 2020 (RF13), overlaid with**
 100 **GOES-16 satellite-measured cloud optical depth (COD) at 15:21 UTC. The insert shows the time series of flight altitude for both**
 101 **aircraft. (b) Time and height of the eight Falcon flight legs within or near the dropsonde array domain. The insert is the horizontal**
 102 **location of the eight flight legs and the dropsonde domain (thin black line). Acronym of flight leg types: BCB: below cloud base;**
 103 **ACB: above cloud base; ACT: above cloud top; BCT: below cloud top; MinAlt: minimum altitude (~120 m above ground level**
 104 **(AGL)).**

105 2.2 Forcing and Evaluation Data

106 Table 1 lists the aircraft measurements used in this study. These observational data are used mainly for two purposes: driving
 107 models as initial and boundary conditions and evaluating model results. Satellite measurements and reanalysis data are also
 108 used to supplement the aircraft measurements to give a more complete view and fill data gaps when aircraft data are
 109 unavailable. Specifically, the liquid water path (LWP) and the ice water path (IWP) are retrieved from GOES-16
 110 geostationary satellite using the Visible Infrared Solar-Infrared Split Window Technique (VISST) (Minnis et al., 2008;
 111 Minnis et al., 2011) algorithm from the NASA-Langley Satellite Cloud Observations and Radiative Property retrieval
 112 System (SatCORPS). ERA5 reanalysis (Hersbach et al., 2020) is used to provide model initial and boundary conditions to
 113 drive the WRF-CRM simulation, and to supplement the large-scale forcing used by WRF-LES and E3SM-SCM. More
 114 details of the large-scale forcing are given in the next subsection.

115
 116 **Table 1: Aircraft measurements used in this study.**

Instrument	Measurements	Platform	Data Version
GPS	Flight location (lat, lon, alt)	Falcon	R4
N/A	Flight leg flag	Falcon	R3
Five-port pressure system (TAMMS)	3-D winds	Falcon	R4
Rosemount 102 sensor	Temperature	Falcon	R4
Diode laser hygrometer (DLH)	Water vapor mixing ratio	Falcon	R1
Scanning Mobility Particle Sizer (SMPS)	Aerosol number size distribution (2.97 – 94.0 nm)	Falcon	R4
Laser Aerosol Spectrometer (LAS)	Aerosol number size distribution (93.9 – 3487.5 nm)	Falcon	R3
High-Resolution Time-of-Flight Aerosol Mass Spectrometer (AMS)	Mass concentration of aerosol composition (Organic, Sulphate, Nitrate, Ammonium, Chloride)	Falcon	R2
Cloud Condensation Nuclei (CCN) Counter	CCN number concentration with supersaturation (SS) scanning from ~ 0.16% to 0.72%	Falcon	R0
Fast Cloud Droplet Probe (FCDP)	Cloud droplet number size distribution (3 – 50 μm), liquid water content (LWC), droplet number concentration and effective radius	Falcon	R1
GPS	Flight location (lat, lon, alt)	King Air	R0
High Spectral Resolution Lidar (HSRL-2)	Cloud top height	King Air	R0
Dropsonde (Vömel et al., 2023)	Temperature, pressure, altitude, relative humidity, U	King Air	R1



	wind, V wind		
--	--------------	--	--

117 **2.3 Model Simulations**

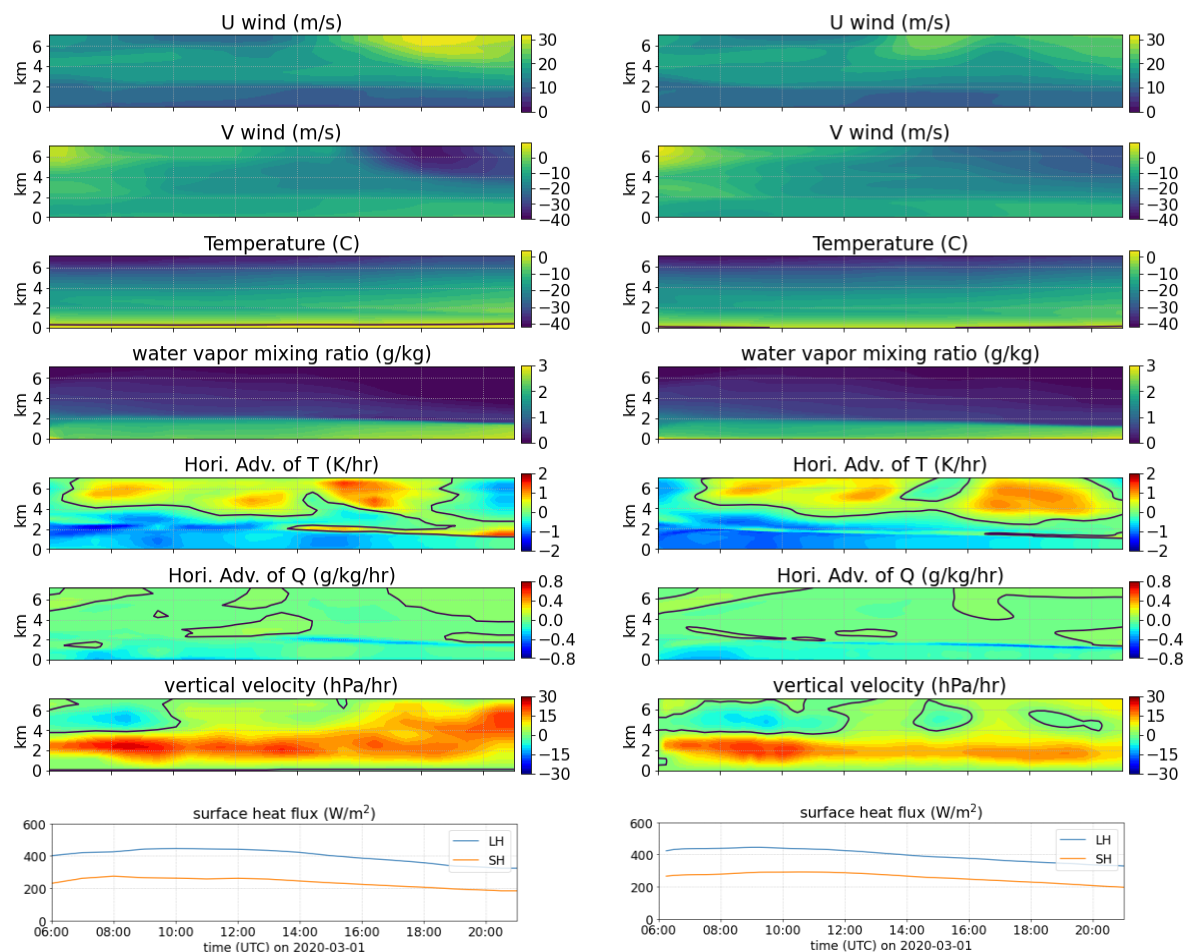
118 The SCM used in this study is based on the Energy Exascale Earth System Model (E3SM) version 2 (Golaz et al., 2022;
119 Bogenschütz et al., 2020). It includes a deep convective parameterization from Zhang and McFarlane (1995) with
120 modification from Xie et al. (2019) to improve diurnal cycle of precipitation, a two-moment microphysics from Gettelman
121 and Morrison (2015) (MG2), and a Cloud Layers Unified By Binormals (CLUBB) (Golaz et al., 2002; Larson and Golaz,
122 2005) parameterization for turbulence, shallow convection and macrophysics all-together. Some parameters of these
123 schemes were systematically re-tuned to improve the overall performance of subtropical stratocumulus clouds (Ma et al.,
124 2022). Aerosols generally require long spin-up time that is unrealistic during the relatively short SCM case durations. Instead
125 of directly use the aerosol scheme, three options has been implemented in E3SM-SCM to treat aerosols: specifying droplet
126 and ice number concentrations to “bypass” ACI, using “prescribed” aerosols from a 10-year E3SM climatology simulation
127 under present-day forcing conditions, or using “observed” aerosol information if available (Bogenschütz et al., 2020). The
128 information of three lognormal distribution modes of aerosols (Aitken, accumulation and coarse) is needed in the
129 “prescribed” and “observed” methods to replace the output from the aerosol scheme, which is 3-mode Modal Aerosol
130 Module (MAM3) (Liu et al., 2012) in the E3SM SCM configuration. Note that this differs from the default MAM4 scheme
131 (Liu et al., 2016) in E3SM GCM. The “observed” method currently does not include vertical variation of aerosols (i.e.,
132 observed aerosol information is applied to all vertical layers from the surface to model top). Therefore, to investigate ACI
133 and the impact of aerosol vertical distribution on clouds, we use a “prescribed-observed” hybrid method in this study, in
134 which we replace the prescribed aerosol data with aircraft-measured aerosols or idealized conditions.

135
136 E3SM-SCM is driven by prescribed large-scale forcing data (i.e., advective tendencies and vertical velocity) and surface
137 turbulent fluxes, with a nudging timescale of 3 h to reduce biases in the atmospheric mean state. We use the same forcing
138 data as Li et al. (2022) in their WRF-LES simulations over the dropsonde region (red circle in Fig. 1a). The large-scale
139 forcing fields are shown in the left panel of Fig. 2. The environment exhibits strong subsidence with cold and dry advection
140 in the lower atmosphere. The near-surface cold and dry air and relatively high SST (not shown) lead to large surface latent (~
141 400 W/m²) and sensible (> 200 W/m²) heat fluxes. Although these data are obtained from the ERA5 reanalysis, which
142 exhibits a cold and dry bias in MBL (Seethala et al., 2021), the wind structure is well captured (Chen et al., 2022) and the
143 ERA5 divergence agrees well with that derived from the ACTIVATE dropsonde array (Li et al., 2022). Overall, it has been
144 shown that the ERA5-derived large-scale forcing and surface turbulent fluxes can reasonably reproduce clouds and boundary
145 layer for this case in WRF-LES simulations (Li et al., 2022; Li et al., 2023).

146
147 The WRF-CRM (Chen et al., 2022) and WRF-LES (Li et al., 2022; Li et al., 2023) simulations are also used for
148 intercomparison with the E3SM-SCM. The WRF-CRM has an outer domain at 3 km horizontal grid and an inner domain in



149 1 km convective-resolving resolution, with an interactive land option and prescribed SST from ERA5. It is able to reproduce
150 the “cloud street” feature seen in satellite images (Chen et al., 2022). Over the dropsonde region, the nested WRF-CRM
151 simulation shows stronger cold advection in MBL and weaker subsidence above MBL (the right panel of Fig. 2) than the
152 ERA5 large-scale forcing. The near-surface temperature and moisture in WRF-CRM are lower than ERA5, yielding higher
153 surface latent (21–68 W/m² higher) and sensible (26–55 W/m² higher) heat fluxes. The WRF-LES simulation has a domain
154 size of 60x60 km² with a 300 m horizontal grid spacing (Li et al., 2022). Its large-scale forcing and surface turbulent fluxes
155 are prescribed from ERA5, as described above. Nudging is applied only to horizontal winds at a timescale of 1 h, with
156 temperature and moisture freely evolving. In both CRM and LES simulations, a uniform cloud droplet number concentration
157 (N_d) was specified so ACI processes are bypassed. The specified N_d value of 450 cm⁻³ was obtained from a previous version
158 of FCDP measurements (Li et al., 2022). The newer version of FCDP (see Table 1) with an update instrument calibration
159 gives a smaller N_d value. As will be seen later (e.g., Fig. 5), E3SM-SCM simulation is more consistent with the updated
160 FCDP data. Note that here we keep the original setups of prescribed N_d in CRM and LES for consistency with previous
161 studies (Chen et al., 2022; Li et al., 2022; Li et al., 2023). As all the simulations are available for the same case, we have the
162 opportunity to demonstrate the value of combining CRM and LES with SCM for process-level understanding of ACI.



ERA5

WRF-CRM

163

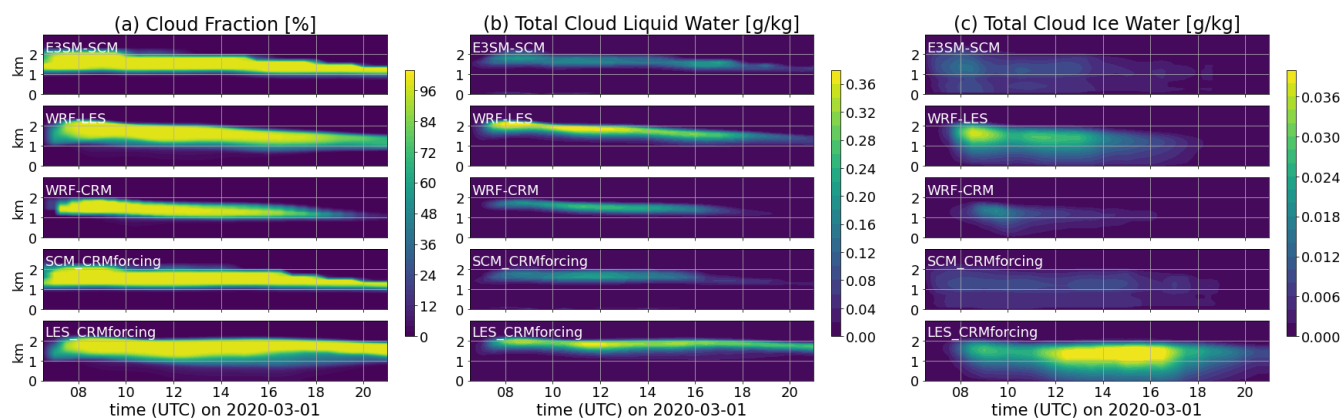
164 **Figure 2: Large-scale environmental conditions, large-scale forcing (horizontal advection and vertical velocity), and surface**
 165 **forcings (latent and sensible heat fluxes) over the dropsonde region from ERA5 used in SCM and WRF-LES (left) and from the**
 166 **WRF-CRM simulations (right). The black lines in large-scale forcing panels mark the zero contour.**

167 **3 SCM/CRM/LES intercomparison**

168 All the E3SM-SCM, WRF-LES, and WRF-CRM simulations are initiated at 06:00 UTC, 1 March 2020. With a quick initial
 169 spin-up, marine CAO clouds develop between 1 and 2 km above ground level (AGL), then display a gradual reduction in
 170 vertical extent, cloud top height, and cloud water content (Figs. 3 and 4). Both SCM and WRF-LES generate a 100% cloud
 171 fraction most of the time, while the WRF-CRM simulated cloud fraction decreases with time. This is associated with the
 172 success of capturing cloud roll structure in WRF-CRM (Chen et al., 2022). However, this roll structure fails to be simulated
 173 in WRF-LES and is neither resolved nor parameterized at the sub-grid scale in E3SM-SCM. Both liquid and ice



174 hydrometeors are produced and transformed into rain and snow particles. The total ice (including snow) water content is
 175 about one order of magnitude smaller than total liquid water (including rain) (Fig. 3). In our further analyses, we ignore ice
 176 and only focus on liquid clouds for simplicity. All simulations produce a weak mean surface precipitation of less than 2
 177 mm/day (Fig. 4b), except an LES sensitivity experiment discussed later. The evaluation of surface precipitation versus
 178 observations is not conducted here due to the lack of surface measurements and the limited ability of satellite measurements
 179 in detecting weak precipitation from low-level MBL clouds (e.g., Battaglia et al., 2020).

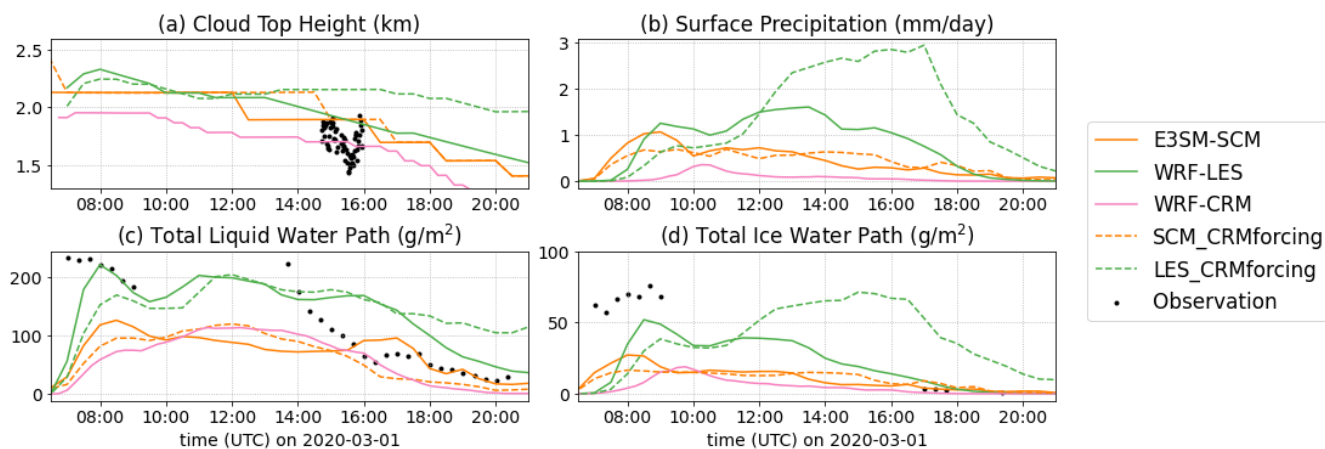


180

181 **Figure 3: Time-height cross-sections of cloud fraction, total liquid water, and total ice water produced from different model**
 182 **simulations.**

183

184 Figure 4a shows the time series of cloud top height compared with HSRL-2 measurements from the King Air aircraft. The
 185 cloud top heights in models are derived by integrating cloud-fraction-weighted height levels downward, as described in
 186 Varble et al. (2023). E3SM-SCM and WRF-LES produce similar cloud top heights (Fig. 4a), consistent with the highest
 187 observed cloud tops but a few hundred meters higher than most of the aircraft in-situ observations during the time of
 188 operation. It should be noted that HSRL-2 detects the top of each individual cloud, which is usually lower than or, at best,
 189 equal to the highest cloud top within the area. Therefore, this result indicates that cloud top height is reasonably simulated in
 190 the three models, although the HSRL-2 measurements indicate a strong spatial variability. Ignoring the model spin-up period
 191 and high solar zenith angle when satellite retrievals encounter large biases, E3SM-SCM and WRF-CRM also reproduced
 192 total liquid path, while WRF-LES overestimates it by ~50% after 14:00 UTC, compared to the satellite retrievals (Fig. 4c).
 193 For the total ice water (including snow), with only a few valid data points in GOES-16 retrievals, SCM and LES seem to
 194 overestimate it, albeit the overall magnitude is small (Fig. 4d).



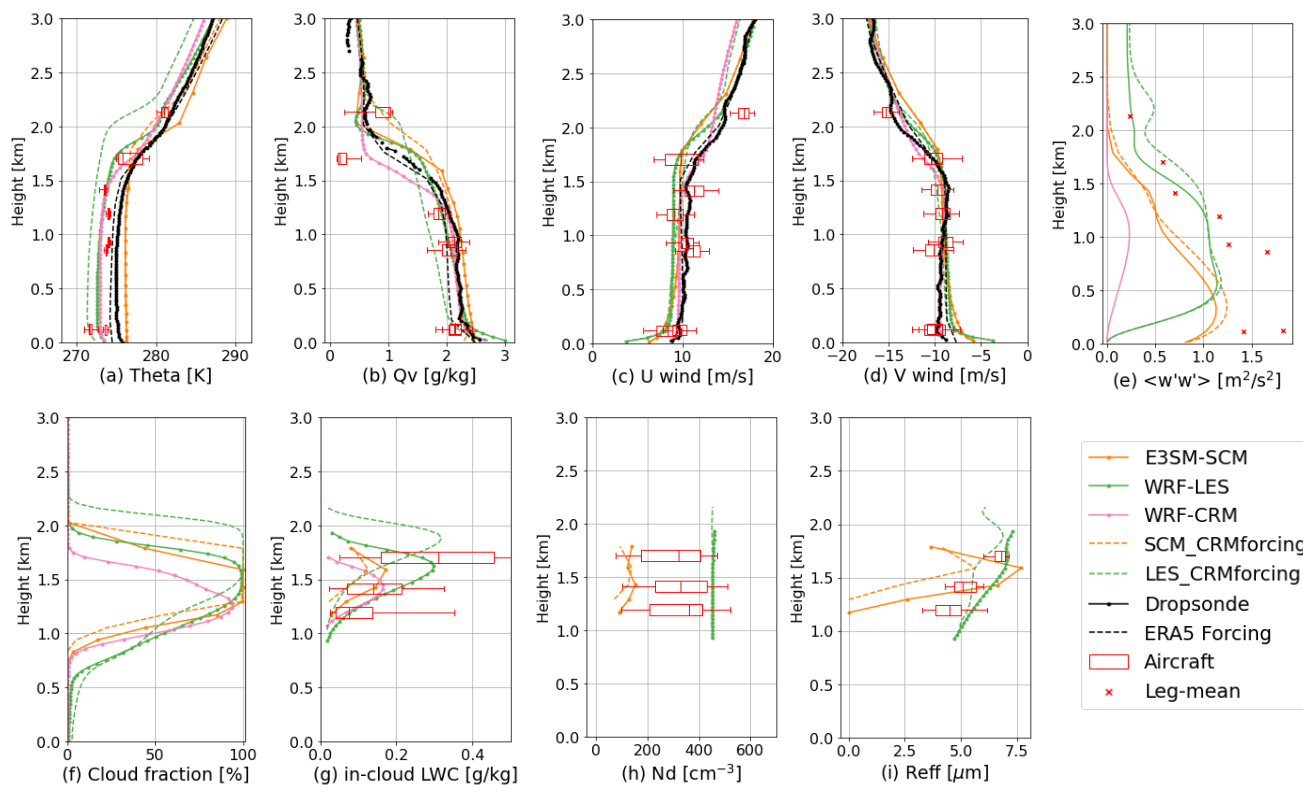
195

196

197

198

Figure 4: Time series of model simulations (lines) compared with observation (dots) for the 01 March 2020 case. Observational data are from the King Air HSRL-2 for cloud top height and GOES-16 retrievals for total liquid (including rain) and total ice (including snow) water paths, for which data points at solar zenith angle greater than 65° are removed.



199

200

201

202

203

204

205

Figure 5: Vertical profiles of atmospheric state, vertical velocity variance and cloud variables over the analysis domain compared with dropsonde and Falcon measurements. Model profiles are averaged between 15:00 and 16:00 UTC during the aircraft measurements. The box plots indicate the interquartile ranges of the aircraft measurements in each flight leg and the whiskers indicate 5th and 95th percentiles, while the red crosses represent vertical velocity variances calculated from 1 Hz measurements in each flight leg. For cloud microphysical variables, a threshold of in-cloud liquid water content of 0.02 g/m^3 and cloud droplet number of 20 cm^{-3} is applied for both model results and aircraft measurements.



206 Figure 5 shows the vertical profiles of atmospheric state and cloud variables compared to dropsondes, ERA5 forcing data,
207 and in-situ aircraft measurements. The atmospheric state variables are constrained by ERA5 reanalysis, which has a colder
208 and dryer boundary layer than the dropsonde measurements (Figs. 5a and 5b, as well as reported in Seethala et al., 2021).
209 However, the Falcon data in the boundary layer are also colder and dryer than the dropsonde measurements. These
210 differences reflect observational uncertainties to some extent. All models are generally consistent with the observations.
211 However, they do show different temperature biases: E3SM-SCM tends to be warmer while WRF-LES and WRF-CRM tend
212 to be colder than the dropsondes. This bias is seen throughout the entire simulation period (not shown), indicating different
213 performances of model parameterizations in E3SM-SCM and WRF-LES, as they used the same initial conditions and large-
214 scale forcing.

215
216 WRF-LES and WRF-CRM both use prescribed N_d obtained from a previous version of Falcon aircraft measurements during
217 the ACB flight leg, which is higher than the re-calibrated value in the current version (Fig. 5h). They produce similar in-
218 cloud liquid water content (LWC) below 1.5 km, but WRF-CRM produces lower LWC above 1.5 km because of its lower
219 cloud top height (Fig. 5g). WRF-LES produces slightly greater droplet effective radius (R_{eff}) than aircraft measurements
220 (Fig. 5i). Together with the large N_d , both contribute to large cloud LWC and LWP. WRF-CRM uses bulk microphysics and
221 does not have R_{eff} . The E3SM-SCM simulated LWC is consistent with aircraft measurements during the BCT2 flight leg
222 near 1.4 km AGL, but lower than the other two in-cloud flight legs (Fig 5g). It also produces larger sizes of cloud droplets
223 around 1.5 km AGL (Fig. 5i), but produces much lower N_d (Fig 5h). The lower N_d is partly due to the smaller vertical
224 velocity variance in the SCM simulations compared to the aircraft measurements (Fig. 5e), suggestive of weaker updraft
225 velocity causing lower supersaturation (SS) which activates fewer cloud condensation nuclei (CCN) into cloud droplets (e.g.,
226 Kirschler et al., 2022). Another reason is the use of climatological aerosols as input, which provides too low CCN
227 concentrations for this case. As will be seen in Sect. 4.1, using observed aerosols brings N_d much closer to the observations.

228
229 The differences in large-scale forcing and surface turbulent fluxes between ERA5 and WRF-CRM (Fig. 2) raise a question
230 of how the large-scale forcing impacts the simulations in E3SM-SCM and WRF-LES, considering that WRF-CRM and
231 E3SM-SCM/WRF-LES show many similarities in simulated cloud properties. To answer this, we configure E3SM-SCM and
232 WRF-LES with the large-scale forcing and surface fluxes from WRF-CRM over the dropsonde domain (shown in the right
233 panel of Fig. 2) to conduct two simulations, referred to as SCM_CRMforcing and LES_CRMforcing, respectively. Results of
234 these two simulations are included as dashed lines in Figs. 3-5. Because of the stronger cold and dry air advection and
235 weaker subsidence, both SCM_CRMforcing and LES_CRMforcing simulations generate a colder, dryer, and deeper
236 boundary layer (Figs. 5a and 5b), especially for LES_CRMforcing in which temperature and moisture are not nudged. The
237 cloud layers in both models are overall thicker than using the ERA5 forcing (Fig. 3a), but detailed features are different
238 between SCM and LES. Compared to the E3SM-SCM, SCM_CRMforcing follows the same trend of cloud top reduction
239 rate (Fig. 4a), with a little time lag. Therefore, the cloud grows higher between 15:00 and 16:00 UTC (Fig. 5f) but has



240 smaller LWC and R_{eff} (Figs. 5g and 5i). For LES, the cloud top height in LES_CRMforcing reduces with a slower rate (Fig.
241 4a), causing a ~500 m higher cloud top between 15:00 and 16:00 UTC (Fig. 5f). Because of the colder temperature, more
242 cloud hydrometeors are converted to the ice phase (Figs. 3c and 4d), with more precipitation falling to the ground (Figs. 4b).
243 This sensitivity study shows a large impact of the large-scale forcing and surface fluxes on cloud properties in the SCM and
244 LES simulations. A proper combination of large-scale dynamics, sub-grid scale parameterizations, and model configurations
245 is needed to obtain optimal performance in simulating MBL clouds.

246 4 SCM Sensitivity Tests

247 The previous section suggests that the underestimation of N_d in E3SM may be due to the underestimation of aerosol number
248 concentration in the climatological aerosol input for this CAO case. In this section, we use observed aerosols to drive E3SM-
249 SCM and conduct two sets of sensitivity studies on aerosol number size distribution and composition to investigate how the
250 input aerosol properties impact clouds and the radiative forcings.

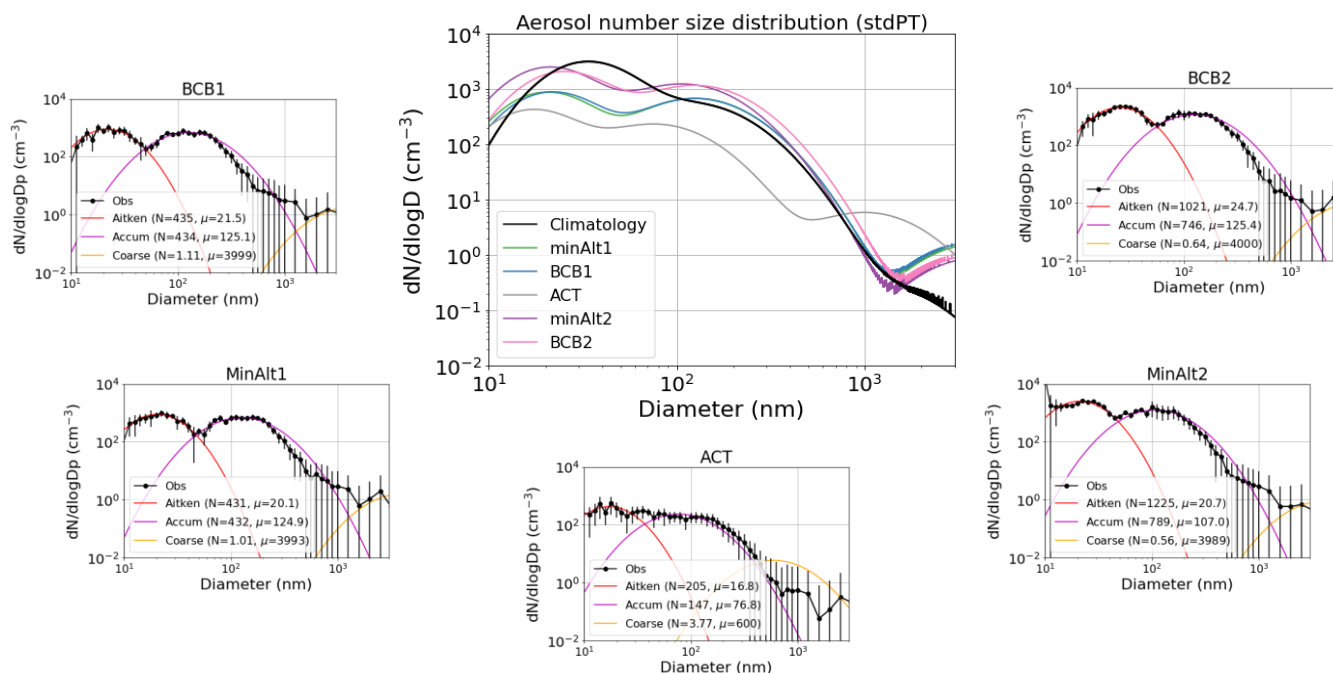
251 4.1 Sensitivity to different aerosol number size distributions

252 We firstly test the sensitivity of SCM simulations to different aerosol number size distributions using the measurements from
253 five out-of-cloud legs within or near the dropsonde domain (Fig. 1b). The Falcon aircraft during ACTIVATE campaign was
254 equipped with an SMPS and an LAS (Table 1) to measure aerosol number size distribution from 2.97 to 94.0 nm (for SMPS)
255 and 93.9 to 3487.5 nm (for LAS), respectively. We merge the two instruments and fit them into three lognormal modes:
256 Aitken, accumulation, and coarse modes. For the three parameters in the lognormal distribution function: mode total number
257 concentration (N), mode geometric median diameter (μ) and standard deviation (σ_g), we only fit N and μ . Because σ_g is also
258 prescribed in other parts of the model (e.g., radiation calculation), we fix σ_g with the E3SM-prescribed values (1.6 for
259 Aitken, 1.8 for accumulation and coarse) for consistency. A sensitivity test shows that using freely fitted N , μ , and σ_g in
260 E3SM-SCM only yields a minor difference compared to using fixed σ_g (not shown). For most flight legs, the fitting of
261 coarse mode aerosols encountered large uncertainties due to too few samples and large variations. As the coarse mode
262 aerosol number concentration is usually orders of magnitude smaller than that of the Aitken and accumulation modes, the
263 poor fitting of coarse mode aerosols is not expected to impact the cloud microphysical properties much.

264
265 The centre panel of Fig. 6 shows the fitted aerosol number size distributions from different flight legs, overlapped with
266 E3SM climatological aerosols near the cloud base height (~900 m AGL). The individual fitting of the three modes as well as
267 the fitting parameters in each flight leg are shown in the surrounding panels. It is clearly seen that the below-cloud flight legs
268 (minAlt and BCB) generally have more aerosols, especially in the accumulation mode, than the above-cloud-top flight leg
269 (ACT). The E3SM climatological aerosols at the BCB2 level show more and larger Aitken mode particles and less coarse
270 mode particles than all flight leg measurements. For accumulation mode particles that are most important for CCN number



271 concentration, the E3SM climatology lies between the ACT leg and below-cloud legs. Although the ACT leg does not
 272 represent cloud-base aerosol conditions that are more relevant to the aerosol activation process, the inclusion of this leg
 273 provides information of how SCM performs in a clean environment.



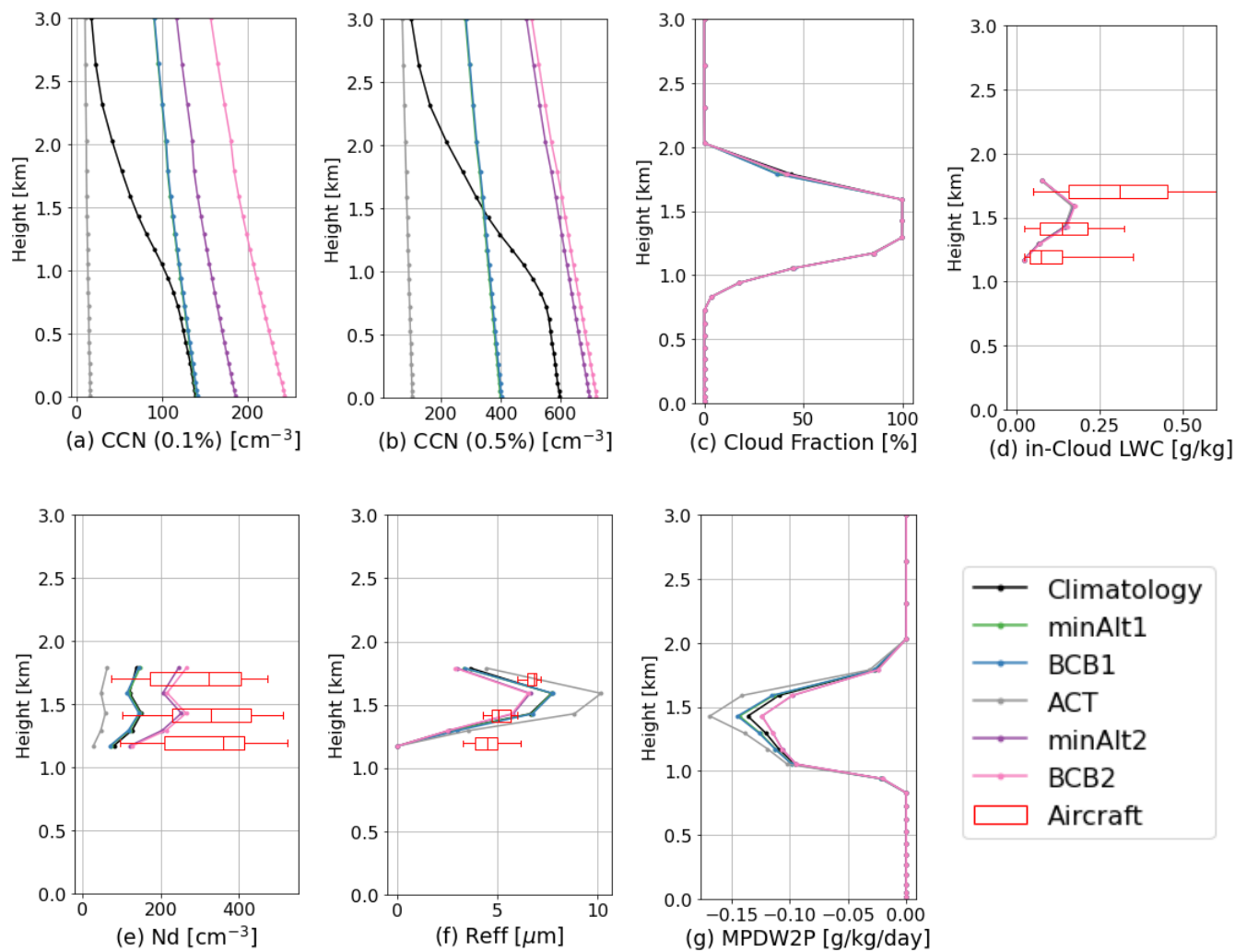
274
 275 **Figure 6:** (centre) Aerosol number size distribution from (black) E3SM prescribed aerosol file from climatological run near the
 276 height of simulated cloud base (~900 m AGL) and (colours) aircraft measurements averaged for each out-of-cloud flight leg fitted
 277 to 3-mode lognormal distributions. (surroundings) Mean observed aerosol number size distribution and one standard deviation
 278 (vertical lines) from each out-of-cloud flight leg and the lognormal fittings for Aitken, accumulation, and coarse modes. The fitting
 279 parameters (N in cm^{-3} and μ in micrometres) are shown in the figure legends with the geometric standard deviation (σ_g) set as 1.6
 280 for Aitken mode and 1.8 for accumulation and coarse modes. All data are converted for standard pressure (1013.25 hPa) and
 281 temperature (273.15 K) conditions.

282 The fitted lognormal parameters from aircraft measurements are used to calculate and replace the variables in the E3SM
 283 prescribed aerosol input data. The averaged chemical component fractions below 1.5 km from E3SM aerosol climatology are
 284 used to partition the measured aerosol number size distribution so they all have the same fraction of aerosol components. The
 285 sensitivity to different aerosol chemical compositions will be discussed in Sect. 4.2, while in this section we only focus on
 286 how aerosol number concentration impacts clouds in E3SM-SCM. The prescribed aerosol concentration has no information
 287 of variation with height. This height-independent assumption is usually used in SCM configurations with observed aerosols
 288 (e.g., Liu et al., 2007; Klein et al., 2009; Liu et al., 2011), assuming that only cloud-base aerosols are involved in the cloud
 289 droplet nucleation processes (e.g., Liu et al., 2011). Nonetheless, we also conduct a sensitivity study on aerosol vertical
 290 distributions in Sect. 4.3.

291



292 Figure 7 (a-f) shows the vertical profiles of aerosol and cloud properties from the E3SM-SCM aerosol sensitivity simulations
293 between 15:00 and 16:00 UTC. The large variation of CCN number concentration has a very small impact on the cloud
294 fraction and in-cloud LWC. Instead, it mainly impacts the cloud droplet number and size: more CCN number concentration
295 leads to more N_d and smaller droplet size. However, all the simulations underestimate N_d compared to the aircraft
296 measurements. As seen in Fig. 8, the gamma distribution assumption of the cloud droplet spectrum in MG2 generally
297 captures the observed droplet size distribution and reproduces well the mean droplet size, but fails to reproduce the observed
298 peak of N_d at all three heights. A similar sharp peak of N_d around 10 to 20 μm was also observed by aircraft over the
299 Southern Ocean and the model with the same MG2 microphysics scheme underestimated N_d in a similar way (Gettelman et
300 al., 2020). Since observed aerosols are used to drive the SCM simulations, the underestimation of N_d indicates that the
301 turbulence in SCM is likely too weak that produces lower supersaturation thus cannot activate enough aerosols into cloud
302 droplets. This is confirmed by the evidence that E3SM-SCM underestimates vertical velocity variance when compared to the
303 Falcon measurements (Fig. 5e), and is a general bias seen in the entire ACTIVATE campaign (Brunke et al., 2022).
304



305

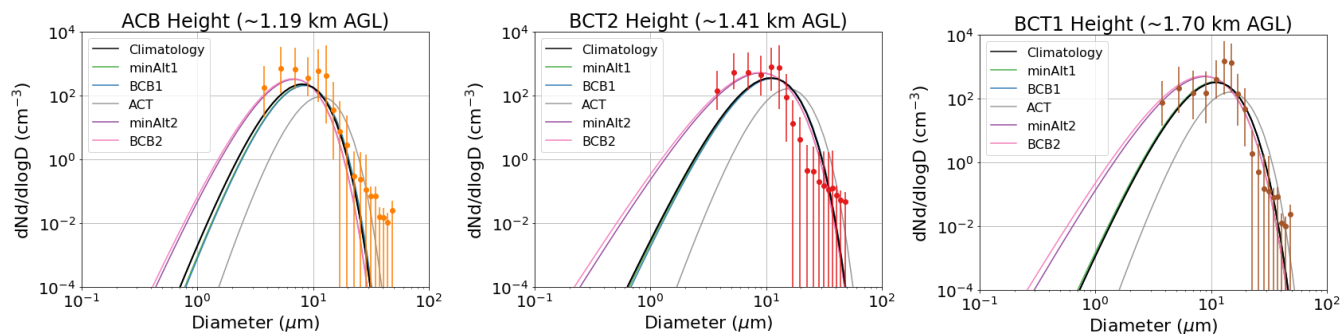
306

307

308

309

Figure 7: Vertical distributions of (a) CCN number concentrations at 0.1% and (b) 0.5% supersaturation, (c) cloud fraction, (d) in-cloud LWC, (e) N_d , (f) R_{eff} , and (g) cloud water tendency from the conversion-to-precipitation processes in E3SM-SCM simulations with different aerosol specifications. Aircraft measurements of cloud microphysical properties overlaid are the same as in Figure 5.



310



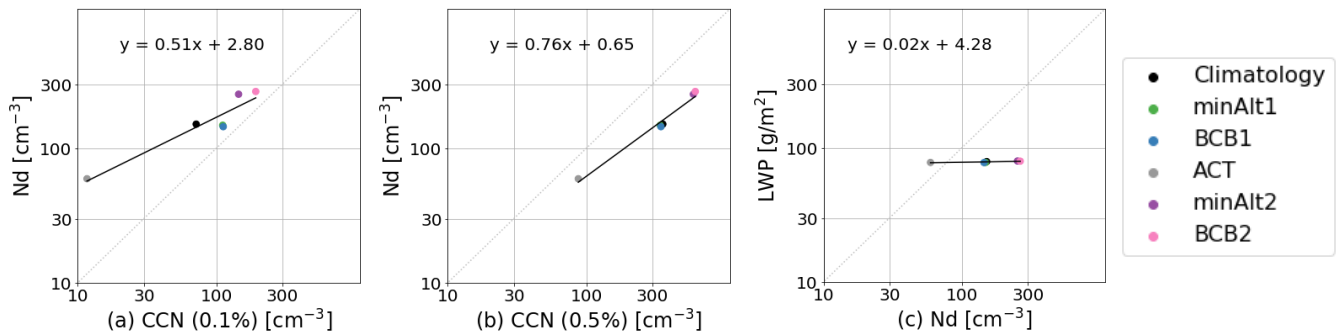
311 **Figure 8: E3SM-SCM simulated cloud droplet size distribution at the height of three in-cloud flight legs: (ACB: ~1.20 km, BCT2:**
 312 **~1.44 km, BCT1: ~1.74 km). The dots and error bars represent aircraft measurements at the corresponding flight legs and 5th and**
 313 **95th percentiles.**

314

315 The strong impact of aerosol number size distribution on cloud microphysical properties (number, size) in SCM indicates
 316 that E3SM shows a strong Twomey effect (Twomey, 1977, 1959). The change of N_d is tightly related to the change of CCN
 317 number concentration (Fig. 9). A recent study of long-term E3SM simulation over the eastern North Atlantic suggests that
 318 the N_d susceptibility (i.e., $\frac{d\ln N_d}{d\ln CCN}$ relationship) in E3SM may be too strong comparing to observations (Tang et al., 2023).
 319 Previous studies showed that N_d is also impacted by other factors such as updraft velocity (e.g., Kirschler et al., 2022; Chen
 320 et al., 2016), which indicates a potential need of examining updraft velocity in E3SM in the future. The surface downward
 321 shortwave flux is largely impacted by the change of cloud droplet number and size due to different aerosol specifications
 322 (Fig. 10c), with the differences reaching up to 100 W m^{-2} during the analysis period (15:00 – 16:00 UTC).

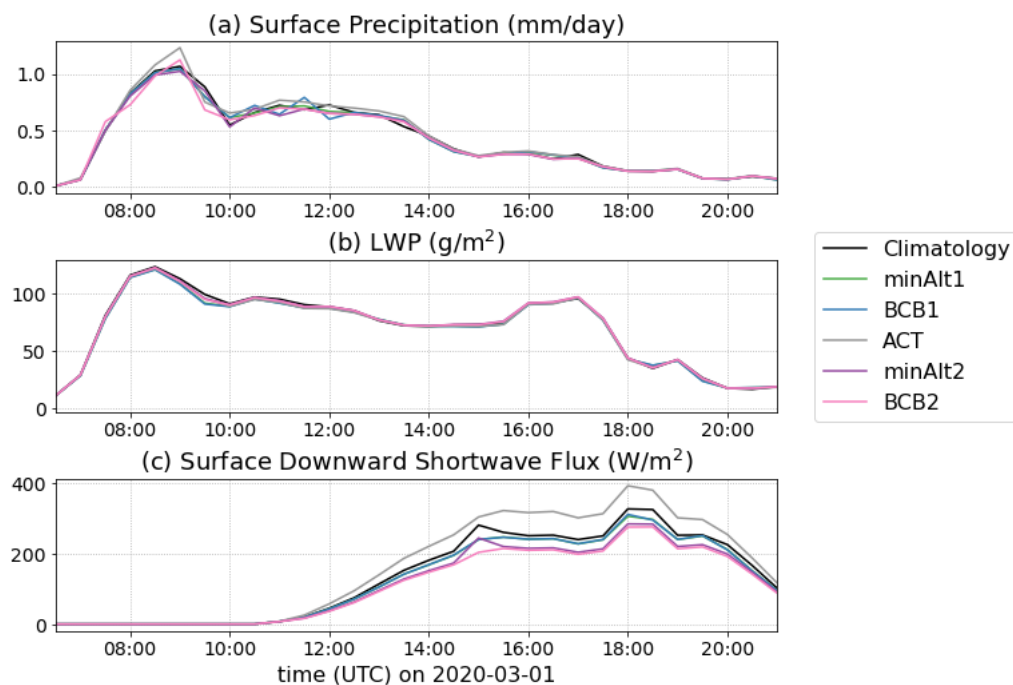
323

324 In contrast to the strong Twomey effect, the weak impact of aerosols on cloud macrophysical properties (cloud fraction, total
 325 water content) indicates a very weak LWP adjustment in E3SM. The LWP susceptibility $\frac{d\ln LWP}{d\ln N_d}$ is almost zero (Fig. 9c). The
 326 slightly positive slope is likely due to the suppression of precipitation processes (Fig. 7g) when cloud droplet sizes decrease
 327 in responses to more aerosol particle and cloud droplet numbers. However, the magnitude of precipitation rate change is so
 328 small that it can barely change the overall LWP and surface precipitation (Fig. 10). This weakly linear $\frac{d\ln LWP}{d\ln N_d}$ relation in the
 329 E3SM-SCM simulations is different with the non-linear $\frac{d\ln LWP}{d\ln N_d}$ relation seen in the long-term E3SM GCM run (Tang et al.,
 330 2023). Whether this weak $\frac{d\ln LWP}{d\ln N_d}$ susceptibility is a case-specific feature, the SCM simulation constrained by large-scale
 331 forcing has a lack of a feedback mechanism, or there is a large LWP – N_d covariance with different thermodynamic
 332 conditions warrants future studies with more SCM cases or long-term simulations.



333

334 **Figure 9: Scatter plot between simulated N_d and CCN at two different supersaturations and between LWP and N_d . The linear fit**
 335 **equations representing $\frac{d\ln N_d}{d\ln CCN}$ and $\frac{d\ln LWP}{d\ln N_d}$ are noted in each panel.**



336

337

338

Figure 10: Time series of (a) surface precipitation, (b) LWP, and (c) surface downward shortwave flux from E3SM-SCM simulations with different aerosol specifications.

339

4.2 Sensitivity to different aerosol composition

340

341

342

343

344

345

346

347

348

349

350

351

352

353

354

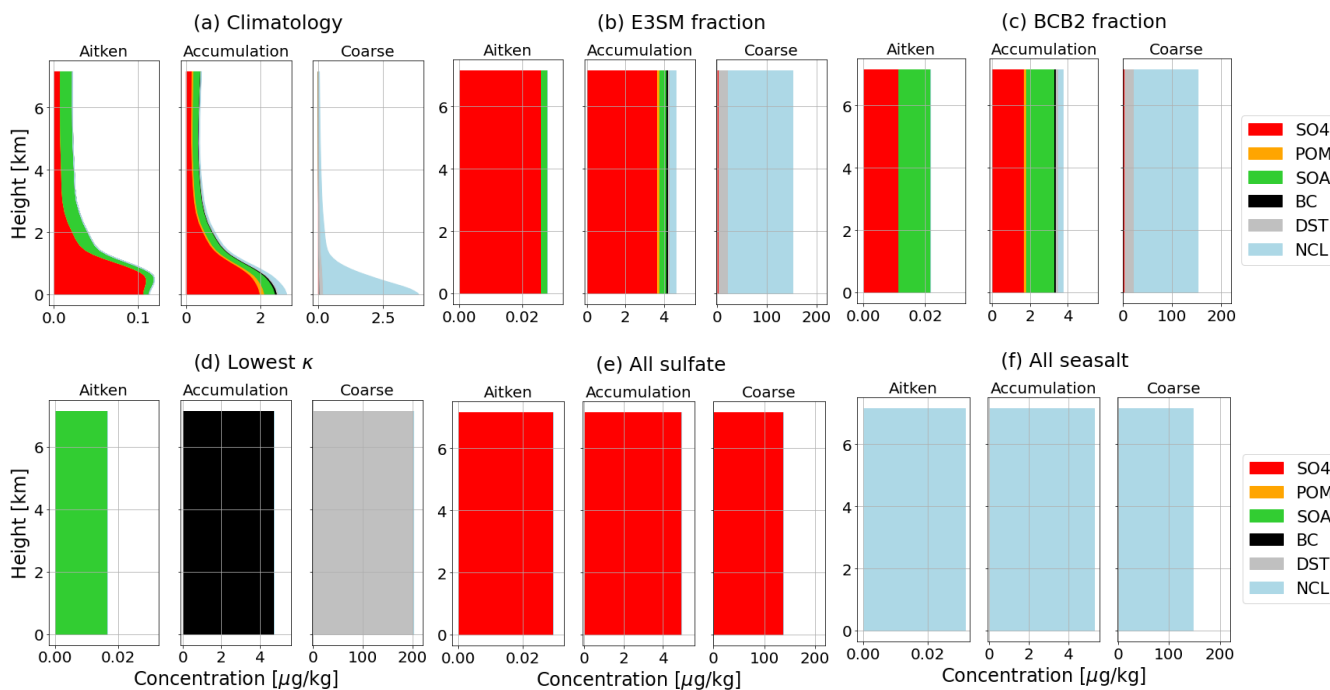
Aerosol chemical composition is an important property that determines the aerosol hygroscopicity (κ) and further impacts the likelihood of aerosols serving as CCN and being activated into cloud droplets. In E3SM, the overall κ is calculated assuming internal mixing of aerosol species within each mode and external mixing among modes (Liu et al., 2012; Liu et al., 2016). Although aerosol chemical composition also impacts the overall size distribution (Shrivastava et al., 2017), this mechanism is not implemented in the current E3SM. In this section, we investigate the differences of aerosol composition used in E3SM and observed by Falcon aircraft measurements, and further test the sensitivity of simulated clouds to aerosol composition using simulated and observed values and assuming a few extreme conditions, focusing on the change of hygroscopicity.

Figure 11a shows the aerosol mass concentrations for each component in the E3SM aerosol climatology. Most of the aerosols are concentrated within the boundary layer below 1 km, with the Aitken and accumulation modes dominated by sulphate, and the coarse mode dominated by sea salt aerosols. Figures 11 (b-f) all use the same observed aerosol number size distribution, fitted from the BCB2 flight leg, but combined with different aerosol component fractions. The setting of “E3SM fraction” uses aerosol composition from E3SM prescribed aerosols at the level closest to the BCB2 leg (near ~900 m AGL). The “BCB2 fraction” uses aerosol composition from the AMS measurements at the BCB2 leg. Among the five components



355 in AMS measurements (Table 2), sulphate (SO₄) and organics are the two dominated species observed during ACTIVATE
 356 (Dadashazar et al., 2022a). They are also the only two species specified in E3SM, with assumptions of the composition of
 357 organics. Here we assume all AMS measured organics are secondary organic aerosols (SOA), then calculate new aerosol
 358 concentrations using the observed mass fraction of SO₄ and SOA while keeping the fraction of other species the same in
 359 E3SM. It can be seen that the aircraft measured SO₄:SOA ratio is about 1:1 in mass, much smaller than in the E3SM
 360 climatology. This change results in a reduction of κ value from 0.46 to 0.31 (Table 2) as the hygroscopicity of SOA is much
 361 smaller than SO₄.

362
 363 Three other idealized aerosol settings in extreme conditions are provided for the purpose of sensitivity test. The first one,
 364 “Lowest κ ”, is the option to use the lowest hygroscopicity species in each mode. The second option assumes all aerosols are
 365 SO₄ aerosols and the third one assumes all sea salt aerosols. The corresponding aerosol fraction in each mode and the overall
 366 κ values are given in Table 2. The “Lowest κ ” option has an extremely low κ value of 10^{-10} in the accumulation mode, while
 367 the “all seasalt” option has a large κ of 1.16. The other options have κ values varying from 0.3 to 0.5.



368
 369 **Figure 11: Different settings of aerosol mass concentration for each component used in E3SM from (a) climatology from E3SM**
 370 **GCM output, (b) applying composition fraction from E3SM climatology aerosols at the height of BCB2 flight leg, (c) using**
 371 **observed fraction of sulphate and organics (assuming SOA) from the BCB2 flight leg, (d-f) assuming all aerosols are the lowest**
 372 **hygroscopicity species (“Lowest κ ”) in that mode, sulphate and sea salt aerosols, respectively. Note the different x-axis in panel (a)**
 373 **and (b)-(f). In (b)-(f), the aerosol number size distributions are from aircraft measurements in the BCB2 flight leg and assuming**
 374 **no vertical variation. Notation of aerosol species: SO₄: sulphate, POM: primary organic matter, SOA: secondary organic aerosols,**
 375 **BC: black carbon, DST: dust, NCL: sea salt.**



376
377

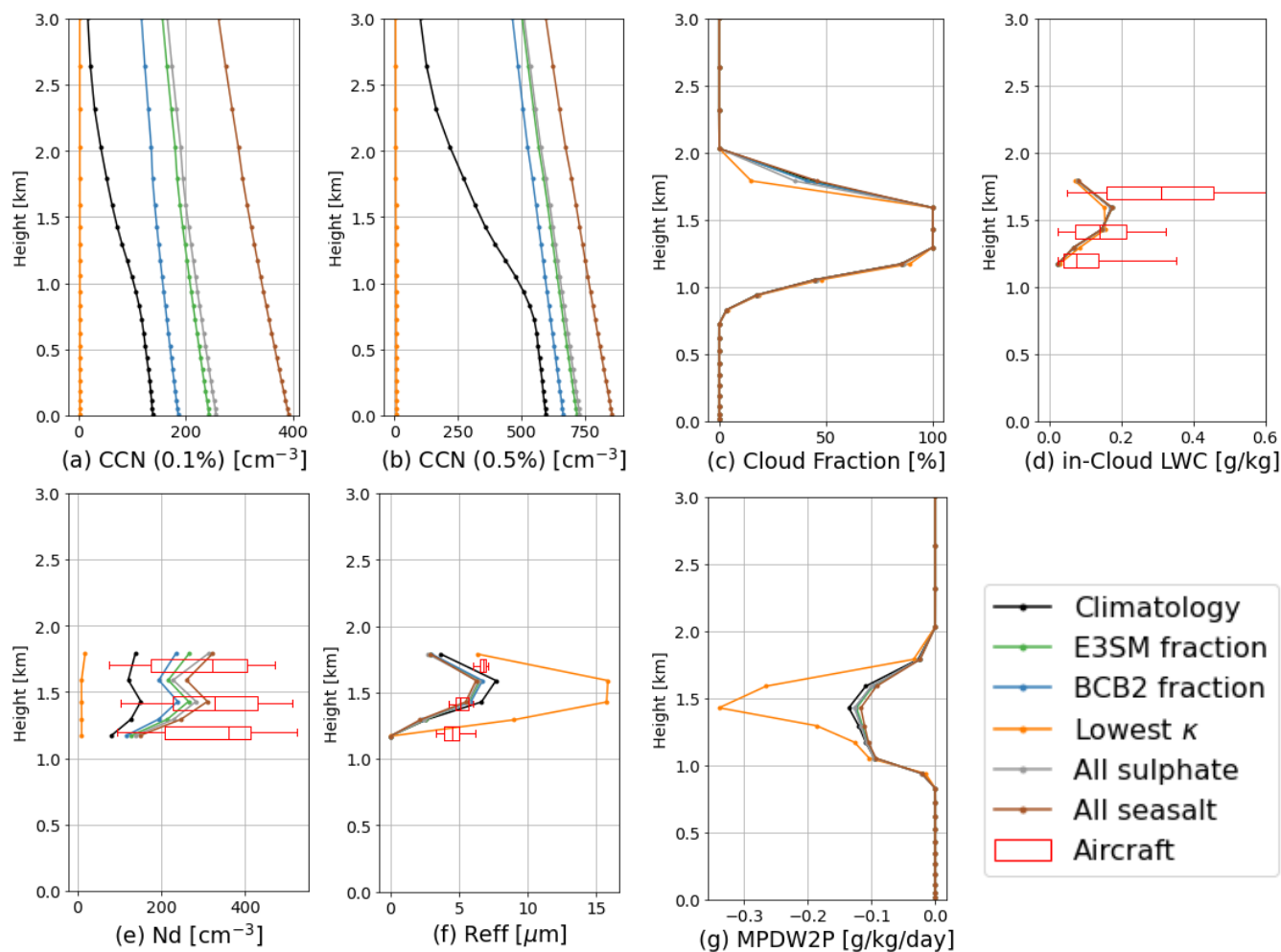
Table 2: Fraction of aerosol species in each mode (Aitken/accumulation/coarse modes) specified in five sensitivity tests. “-” means the species is not accounted for in the mode.

Sensitivity test	SO ₄	POM	SOA	BC	DST	NCL	κ^*
E3SM fraction	0.89/0.75/0.02	-/0.04/-	0.11/0.12/-	-/0.02/-	-/0.02/0.09	0.00/0.05/0.88	0.46
BCB2 fraction	0.39/0.34/0.02	-/0.04/-	0.61/0.53/-	-/0.02/-	-/0.01/0.09	0.00/0.05/0.88	0.31
Lowest κ	0/0/0	-/0/-	1/0/-	-/1/-	-/0/1	0/0/0	10⁻¹⁰
All sulphate	1/1/1	-/0/-	0/0/-	-/0/-	-/0/0	0/0/0	0.507
All seasalt	0/0/0	-/0/-	0/0/-	-/0/-	-/0/0	1/1/1	1.16

378 * : κ is calculated from the accumulation mode.

379

380 The different aerosol hygroscopicity results in different CCN number concentrations (Fig. 12a and 12b). As SS increases, the
 381 critical diameter determining CCN number concentration decreases and becomes less sensitive to hygroscopicity. Therefore,
 382 except the “Lowest κ ” sensitivity run in which the CCN number concentration is almost zero, the relative difference of CCN
 383 number concentration with different aerosol composition settings is smaller for 0.5% SS than 0.1% SS. N_d and R_{eff} are less
 384 sensitive to aerosol hygroscopicity ranging from 0.31 to 1.16 compared to CCN number concentration, and cloud fraction
 385 and LWC vary even less. The only outlier is the “Lowest κ ” option with extremely low hygroscopicity. In this case the
 386 extremely low CCN and N_d number concentration (but not zero, as the E3SM model sets a lower limit of $N_d = 10 \text{ cm}^{-3}$ when
 387 cloud exists) lead to about doubled droplet size (Fig. 12f). Therefore, it has a much stronger surface downward shortwave
 388 radiation (Fig. 13c). The much larger droplet size also contributes to more precipitation conversion (Figs. 12g and 13a) and
 389 depletion of cloud liquid water (Fig. 13b). However, the impact is still very weak and the estimated LWP susceptibility
 390 $\frac{d \ln LWP}{d \ln N_d}$ is 0.02 (Fig. 14c).

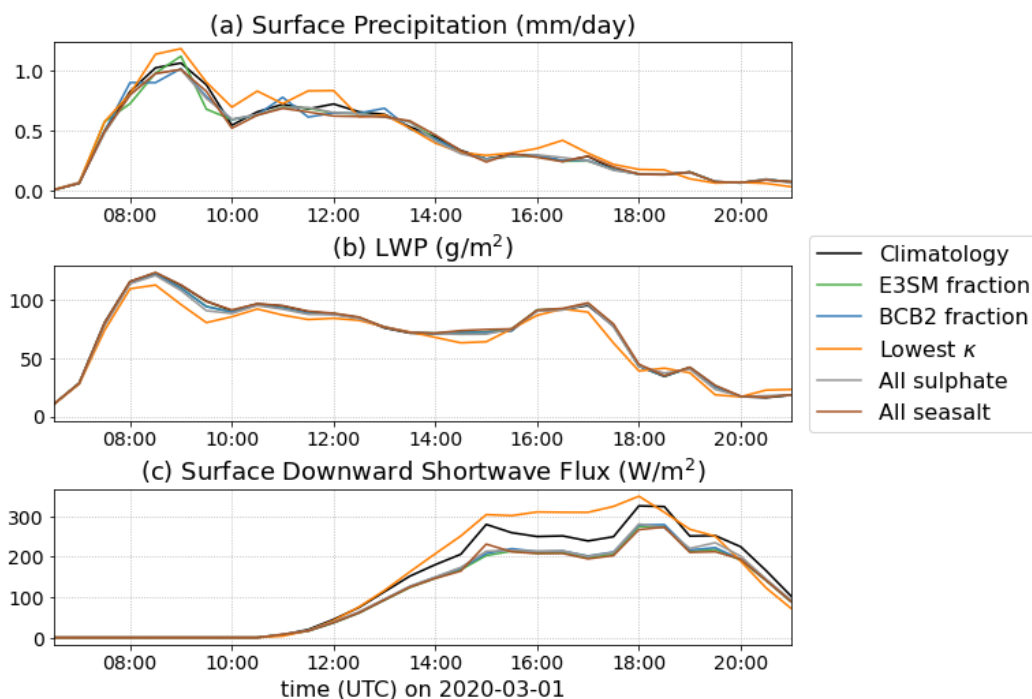


391

392

393

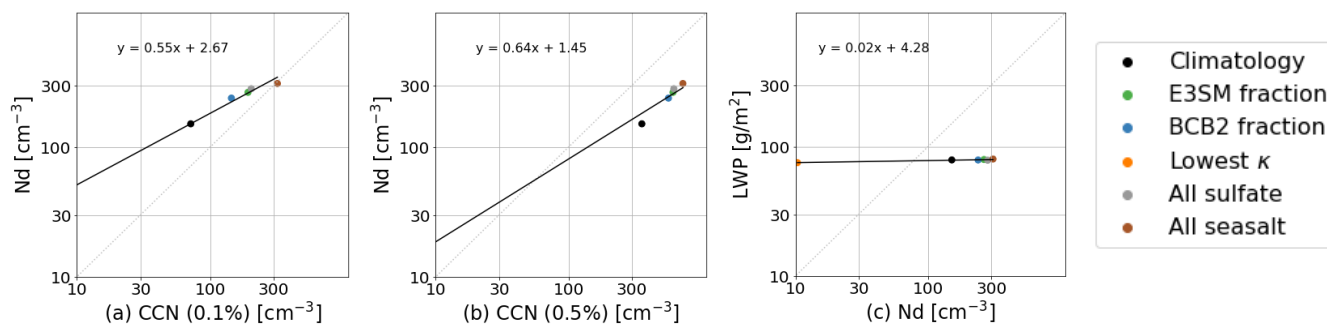
Figure 12: Same as Figure 7 but for E3SM-SCM simulations with different aerosol compositions and same aerosol number concentration (except Climatology) from BCB2 measurements.



394

395

Figure 13: same as Figure 10 but for E3SM-SCM simulations with different aerosol compositions.



396

397

Figure 14: same as Figure 9 but for E3SM-SCM simulations with different aerosol compositions.

398

4.3 Sensitivity to aerosol vertical distribution

399

400

401

402

403

404

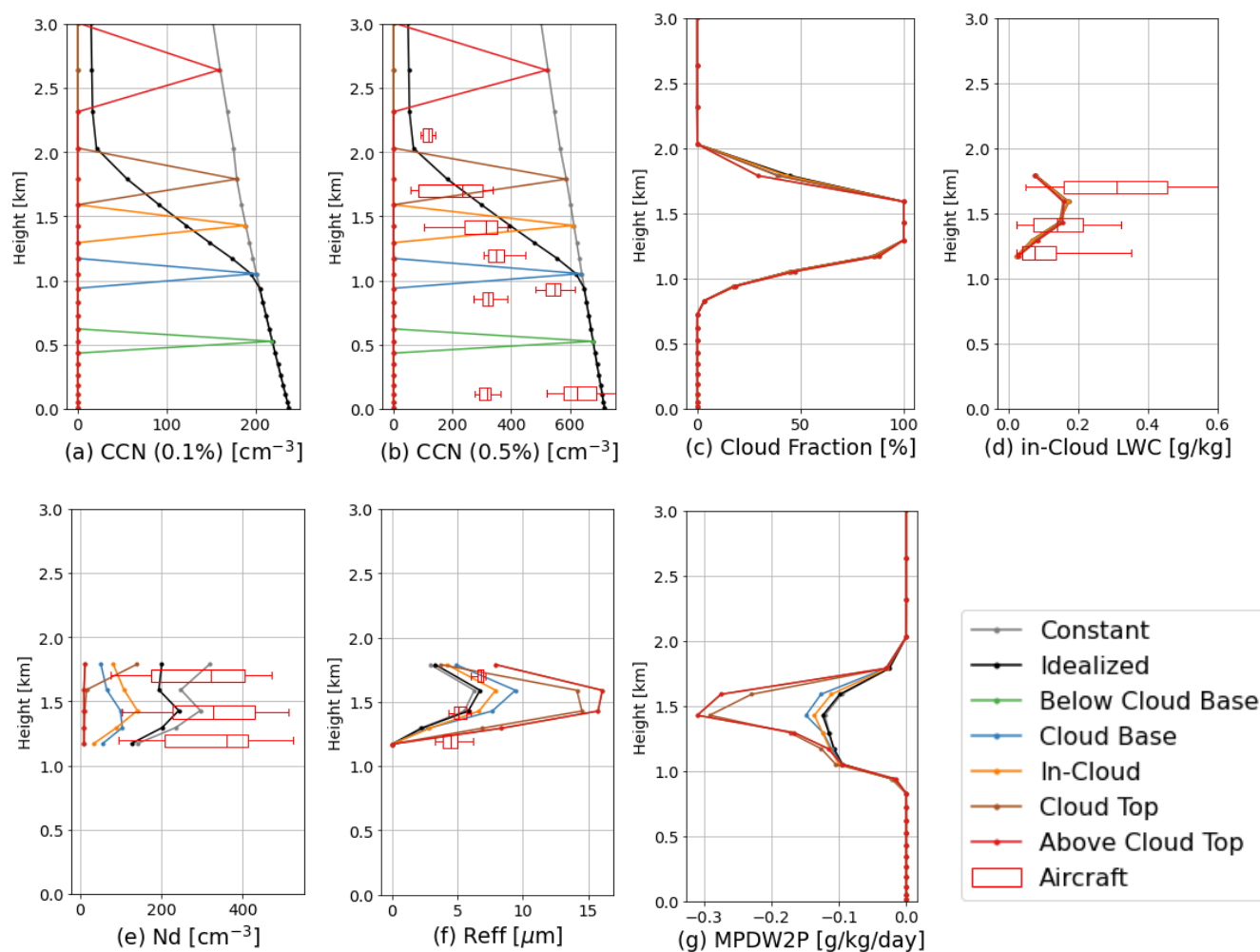
405

In many previous modelling studies using observed aerosols, usually only one set of aerosol parameters (i.e., particle number size distribution and composition) was given to the model regardless of the vertical distribution (Liu et al., 2011; Liu et al., 2007; Klein et al., 2009; Lebassi-Habtezion and Caldwell, 2015; Li et al., 2023). The observed aerosol information is usually taken from in-situ measurements below cloud base (e.g., Liu et al., 2011; Li et al., 2023), assuming that hygroscopic aerosol particles are readily activated into cloud droplets in the saturated air driven by updrafts. However, as aerosol concentration usually decreases with height, the aerosol vertical distribution may be changed by in-cloud scavenging, horizontal transport and vertical mixing, which further affect the cloud microphysical properties (e.g., Lin et al., 2023; Zhang et al., 2021;



406 Kirschler et al., 2022). Indeed, the secondary activation of aerosols above cloud base has been shown to have a significant
407 impact on aerosol convective removal and vertical transport (Wang et al., 2013; Wang et al., 2020). Here we perform a
408 sensitivity study to investigate the impact of aerosols at different vertical levels on E3SM-SCM simulated clouds, and further
409 assess the impact of aerosol vertical distribution on clouds, comparing to results from the simulations with constant vertical
410 aerosol concentration.

411
412 In this set of sensitivity tests, we prescribe aerosols from BCB2 flight leg only for a single model layer, with all other layers
413 being aerosol-free. We also perform a simulation with idealized aerosol vertical distribution, where aerosol number
414 concentration decreases linearly from 1 km to 2 km AGL (approximately within the cloud layer) to 10% of its boundary-
415 layer value. Figure 15 shows the vertical profiles of the simulation results. With a prescribed aerosol configuration, the cloud
416 activation process only takes the aerosol information in that layer. However, when aerosol particles are activated into cloud
417 droplets, they are redistributed vertically via vertical transport and sedimentation. The aerosols below cloud base and above
418 cloud top do not participate in the cloud activation process, with $N_d = 10 \text{ cm}^{-3}$ (the low cut-off value) and large R_{eff} similar to
419 the “Lowest κ ” results in Fig. 12. Aerosols within the “Cloud Base” and “In-Cloud” layers contribute to about 30% to 40%
420 of N_d activated in the “Constant” aerosol run throughout the simulated cloud layer. The “Cloud Top” aerosols mainly
421 contribute to N_d at the cloud-top layer, with a few droplets falling to lower levels causing a reduction in droplet size (Fig.
422 15f). The “Idealized” aerosol profile generally captures the vertical distribution of aircraft measured CCN (Fig. 15b), albeit
423 aircraft measured CCN is overall smaller near the cloud base, likely due to the aerosol scavenging process. Although the
424 decrease of aerosols is 90% at the cloud top, the reduction of N_d in the “Idealized” case is only 20% to 30% less than the
425 “Constant” case (Fig. 15e). Since E3SM-SCM underestimates N_d in this case, it is difficult to demonstrate the value of
426 adding aerosol vertical variation. Moreover, the prescribed-aerosol setting in E3SM-SCM limits its ability to study ACI. An
427 interactive aerosol configuration with vertical transport and other processes such as dry and wet deposition enabled is needed
428 to further understand the impact of aerosol vertical distribution on clouds and ACI.



429

430 **Figure 15:** Same as Figure 7 but for E3SM-SCM simulations with (gray): constant aerosol number concentration (per kg air),
 431 (black): idealized aerosol profile with number concentration decreasing from 1 to 2 km AGL to 10% of the MBL concentration,
 432 and (colours): aerosols in a single layer only. Aircraft measured CCN number concentrations for SS between 0.45% and 0.55%
 433 are overlaid in (b). Aerosol number concentration is from aircraft measurements in the BCB2 leg while aerosol composition is
 434 from E3SM climatology at the BCB2 leg height.

435 **5 Summary and Discussion**

436 Current ESMs remain largely uncertain in simulating MBL clouds, and ACI related to MBL clouds have been underexplored
 437 over the WNAO. With the recent ACTIVATE field campaign conducted over WNAO collecting in-situ and remote-sensing
 438 measurements using dual aircraft flying simultaneously, we perform a model intercomparison and sensitivity study for a
 439 selected CAO case to understand the complex aerosol-cloud interactions related to MBL clouds over WNAO.

440



441 A unique feature of this study is the multi-scale model intercomparison using SCM, CRM and LES models, which provides
442 a comprehensive process-level understanding of ACI in more details compared to individual models. We conducted E3SMv2
443 simulations in the SCM mode, and compared with two WRF model configurations at LES and CRM resolutions,
444 respectively. Overall, the three models all capture the MBL cloud properties, while the E3SM-SCM underestimates cloud
445 droplet number concentration and overestimates droplet size. This is partly due to the relatively low concentration of
446 prescribed aerosols from the E3SM climatology compared to the observation in this case, and partly due to underestimated
447 updrafts that cannot activate enough aerosol particles into cloud droplets. Note that some parameters in E3SMv2 were tuned
448 to improve the overall performance of subtropical stratocumulus clouds (Ma et al., 2022), but turbulence over the WNAO
449 region is weakened comparing to the pre-tuning version (close to E3SMv1) even in a long-term GCM run (Brunke et al.,
450 2022). The evaluation of SCM simulations against the ACTIVATE measurements is helpful for understanding and
451 improving turbulence representation over this region.

452

453 Among the three models, E3SM-SCM and WRF-LES are driven by the same large-scale and surface forcings derived from
454 ERA5 reanalysis, while the WRF-CRM model is run as a regional model with nested-domains. However, only the WRF-
455 CRM reproduces the characteristics of cloud rolls in this cold-air outbreak case (Chen et al., 2022). With the same large-
456 scale and surface forcings from WRF-CRM, which has weaker subsidence and stronger low-level cold and dry air advections
457 than ERA5 forcings, the E3SM-SCM and WRF-LES produce much thicker clouds than WRF-CRM. This indicates that a
458 proper match of large-scale dynamics, sub-grid scale parameterization, and model configurations is needed to obtain optimal
459 model performance.

460

461 Several sets of sensitivity experiments are conducted to examine ACI by changing the prescribed aerosol number size
462 distribution and aerosol composition in E3SM-SCM. Aircraft measurements at different heights are used to provide
463 constraints of the aerosol perturbation. Changing aerosol number size distributions dramatically alters the CCN number
464 concentration, thus largely impacts cloud droplet number concentration and size, further influencing the cloud radiative
465 effect. However, changing aerosol composition only shows dramatic impacts in the extremely low hygroscopicity (κ) setting,
466 where there are only very few aerosols being activated into very large cloud droplets. Changing the overall κ from 0.31 to
467 1.16 has a smaller impact on cloud microphysical properties. Worth noting, the impact of aerosol composition to CCN
468 concentration and cloud microphysics can be larger than shown here as it may also change the aerosol size distribution
469 (Shrivastava et al., 2017).

470

471 In contrast to the clear Twomey effect, the cloud fraction and water content are barely impacted by aerosol perturbations,
472 with a very weak $\frac{d\ln LWP}{d\ln N_d}$ susceptibility of 0.02. The slight positive LWP adjustment is most likely due to the rain suppression
473 effect (Albrecht, 1989) for smaller cloud droplets. This contradicts the non-linear V-shape $\frac{d\ln LWP}{d\ln N_d}$ curve shown in the long-



474 term E3SM GCM run over the Eastern North Atlantic Ocean (Tang et al., 2023; Varble et al., 2023). Whether this weak
475 positive LWP susceptibility is a case or location specific feature and whether SCM can reveal the same cloud susceptibility
476 as GCM does are subject to further study.

477
478 We also performed a sensitivity study to test the impact of aerosol vertical distribution on cloud simulations. Due to the
479 prescribed-aerosol configuration in E3SM-SCM, only aerosols at cloud levels can be activated. Adding aerosol vertical
480 variation (i.e., decreasing concentration with height) reduces the simulated N_d as there are lower concentrations of aerosols in
481 cloudy layers than below cloud base. However, this may not be necessarily better than vertically constant aerosols obtained
482 below cloud base, because there is no treatment of vertical transport of aerosols in the SCM configuration. A more
483 comprehensive SCM simulation with complete vertical transport and other aerosol processes is needed to better simulate
484 ACI and connect field measurements and process-level models with global models.

485 **Data Availability**

486 The ACTIVATE aircraft data and GOES-16 satellite data are available from the NASA ACTIVATE project website
487 (<https://asdc.larc.nasa.gov/project/ACTIVATE>, DOI: 10.5067/SUBORBITAL/ACTIVATE/DATA001). ERA5 reanalysis
488 data are available from the Copernicus Climate Change Service Climate Data Store (CDS) (Hersbach et al., 2023a, b).

489 **Code Availability**

490 The E3SMv2 model is available from the U.S. Department of Energy at <https://doi.org/10.11578/E3SM/dc.20210927.1> and
491 the SCM scripts are revised from the E3SM SCM library (<https://github.com/E3SM-Project/scmlib>). The WRF community
492 model is available from the National Center for Atmospheric Research (NCAR) at <http://www2.mmm.ucar.edu/wrf/users/>.

493 **Author contribution**

494 ST and HW designed the conceptual ideas. AS, HW, and XZ performed the mission planning and supervision. EC, KT, LZ
495 and CV participated in mission operation and data curation. ST conducted the SCM simulations, XYL conducted the WRF-
496 LES simulations, and JC conducted the WRF-CRM simulations. ST performed the analysis and prepared the original
497 manuscript. All co-authors contributed to the reviewing and editing of the manuscript.

498 **Competing interests**

499 AS and HW are members of the editorial board of Atmospheric Chemistry and Physics. Other authors declare that they have
500 no conflict of interest.



501 Acknowledgments

502 This work was supported through the ACTIVATE Earth Venture Suborbital-3 (EVS-3) investigation, which is funded by
503 NASA's Earth Science Division and managed through the Earth System Science Pathfinder Program Office. The Pacific
504 Northwest National Laboratory (PNNL) is operated for the U.S. Department of Energy by Battelle Memorial Institute under
505 Contract DE-AC0576RLO1830. The simulations were performed using resources available through Research Computing at
506 PNNL. University of Arizona investigators were funded by NASA grant no. 80NSSC19K0442. CV was funded by the
507 German Research Foundation DFG within projects SPP-1294 HALO under Vo1504/7-1 and Vo1504/9-1.

508 References

- 509 Albrecht, B. A.: Aerosols, Cloud Microphysics, and Fractional Cloudiness, *Science*, 245, 1227-1230,
510 <https://doi.org/10.1126/science.245.4923.1227>, 1989.
- 511 Battaglia, A., Kollias, P., Dhillon, R., Roy, R., Tanelli, S., Lamer, K., Grecu, M., Lebsock, M., Watters, D., Mroz, K.,
512 Heymsfield, G., Li, L., and Furukawa, K.: Spaceborne Cloud and Precipitation Radars: Status, Challenges, and Ways
513 Forward, *Reviews of Geophysics*, 58, e2019RG000686, <https://doi.org/https://doi.org/10.1029/2019RG000686>, 2020.
- 514 Bock, L., Lauer, A., Schlund, M., Barreiro, M., Bellouin, N., Jones, C., Meehl, G. A., Predoi, V., Roberts, M. J., and Eyring,
515 V.: Quantifying Progress Across Different CMIP Phases With the ESMValTool, *Journal of Geophysical Research:*
516 *Atmospheres*, 125, e2019JD032321, <https://doi.org/https://doi.org/10.1029/2019JD032321>, 2020.
- 517 Bogenschütz, P. A., Tang, S., Caldwell, P. M., Xie, S., Lin, W., and Chen, Y. S.: The E3SM version 1 single-column model,
518 *Geosci. Model Dev.*, 13, 4443-4458, <https://doi.org/10.5194/gmd-13-4443-2020>, 2020.
- 519 Bony, S. and Dufresne, J.-L.: Marine boundary layer clouds at the heart of tropical cloud feedback uncertainties in climate
520 models, *Geophysical Research Letters*, 32, <https://doi.org/https://doi.org/10.1029/2005GL023851>, 2005.
- 521 Brunke, M. A., Ma, P.-L., Reeves Eyre, J. E. J., Rasch, P. J., Sorooshian, A., and Zeng, X.: Subtropical Marine Low
522 Stratiform Cloud Deck Spatial Errors in the E3SMv1 Atmosphere Model, *Geophysical Research Letters*, 46, 12598-12607,
523 <https://doi.org/https://doi.org/10.1029/2019GL084747>, 2019.
- 524 Brunke, M. A., Cutler, L., Urzua, R. D., Corral, A. F., Crosbie, E., Hair, J., Hostetler, C., Kirschler, S., Larson, V., Li, X.-Y.,
525 Ma, P.-L., Minke, A., Moore, R., Robinson, C. E., Scarino, A. J., Schlosser, J., Shook, M., Sorooshian, A., Lee Thornhill, K.,
526 Voigt, C., Wan, H., Wang, H., Winstead, E., Zeng, X., Zhang, S., and Ziemba, L. D.: Aircraft Observations of Turbulence in
527 Cloudy and Cloud-Free Boundary Layers Over the Western North Atlantic Ocean From ACTIVATE and Implications for
528 the Earth System Model Evaluation and Development, *Journal of Geophysical Research: Atmospheres*, 127, e2022JD036480,
529 <https://doi.org/https://doi.org/10.1029/2022JD036480>, 2022.
- 530 Chen, J., Liu, Y., Zhang, M., and Peng, Y.: New understanding and quantification of the regime dependence of aerosol-cloud
531 interaction for studying aerosol indirect effects, *Geophysical Research Letters*, 43, 1780-1787,
532 <https://doi.org/https://doi.org/10.1002/2016GL067683>, 2016.
- 533 Chen, J., Wang, H., Li, X., Painemal, D., Sorooshian, A., Thornhill, K. L., Robinson, C., and Shingler, T.: Impact of
534 Meteorological Factors on the Mesoscale Morphology of Cloud Streets during a Cold-Air Outbreak over the Western North
535 Atlantic, *Journal of the Atmospheric Sciences*, 79, 2863-2879, <https://doi.org/https://doi.org/10.1175/JAS-D-22-0034.1>,
536 2022.
- 537 Corral, A. F., Braun, R. A., Cairns, B., Gorooh, V. A., Liu, H., Ma, L., Mardi, A. H., Painemal, D., Stamnes, S., van
538 Diedenhoven, B., Wang, H., Yang, Y., Zhang, B., and Sorooshian, A.: An Overview of Atmospheric Features Over the
539 Western North Atlantic Ocean and North American East Coast – Part 1: Analysis of Aerosols, Gases, and Wet Deposition
540 Chemistry, *Journal of Geophysical Research: Atmospheres*, 126, e2020JD032592,
541 <https://doi.org/https://doi.org/10.1029/2020JD032592>, 2021.
- 542 Dadashazar, H., Corral, A. F., Crosbie, E., Dmitrovic, S., Kirschler, S., McCauley, K., Moore, R., Robinson, C., Schlosser, J.
543 S., Shook, M., Thornhill, K. L., Voigt, C., Winstead, E., Ziemba, L., and Sorooshian, A.: Organic enrichment in droplet



544 residual particles relative to out of cloud over the northwestern Atlantic: analysis of airborne ACTIVATE data, Atmos.
545 Chem. Phys., 22, 13897-13913, <https://doi.org/10.5194/acp-22-13897-2022>, 2022a.

546 Dadashazar, H., Crosbie, E., Choi, Y., Corral, A. F., DiGangi, J. P., Diskin, G. S., Dmitrovic, S., Kirschler, S., McCauley, K.,
547 Moore, R. H., Nowak, J. B., Robinson, C. E., Schlosser, J., Shook, M., Thornhill, K. L., Voigt, C., Winstead, E. L., Ziemba,
548 L. D., and Sorooshian, A.: Analysis of MONARC and ACTIVATE Airborne Aerosol Data for Aerosol-Cloud Interaction
549 Investigations: Efficacy of Stairstepping Flight Legs for Airborne In Situ Sampling, Atmosphere, 13, 1242, 2022b.

550 Gettelman, A. and Morrison, H.: Advanced Two-Moment Bulk Microphysics for Global Models. Part I: Off-Line Tests and
551 Comparison with Other Schemes, Journal of Climate, 28, 1268-1287, <https://doi.org/10.1175/jcli-d-14-00102.1>, 2015.

552 Gettelman, A., Bardeen, C. G., McCluskey, C. S., Järvinen, E., Stith, J., Bretherton, C., McFarquhar, G., Twohy, C.,
553 D'Alessandro, J., and Wu, W.: Simulating Observations of Southern Ocean Clouds and Implications for Climate, J. Geophys.
554 Res. Atmos., 125, e2020JD032619, <https://doi.org/10.1029/2020JD032619>, 2020.

555 Golaz, J.-C., Larson, V. E., and Cotton, W. R.: A PDF-Based Model for Boundary Layer Clouds. Part I: Method and Model
556 Description, J. Atmos. Sci., 59, 3540-3551, [https://doi.org/10.1175/1520-0469\(2002\)059<3540:apbmf>2.0.co;2](https://doi.org/10.1175/1520-0469(2002)059<3540:apbmf>2.0.co;2), 2002.

557 Golaz, J.-C., Van Roekel, L. P., Zheng, X., Roberts, A. F., Wolfe, J. D., Lin, W., Bradley, A. M., Tang, Q., Maltrud, M. E.,
558 Forsyth, R. M., Zhang, C., Zhou, T., Zhang, K., Zender, C. S., Wu, M., Wang, H., Turner, A. K., Singh, B., Richter, J. H.,
559 Qin, Y., Petersen, M. R., Mamejtanov, A., Ma, P.-L., Larson, V. E., Krishna, J., Keen, N. D., Jeffery, N., Hunke, E. C.,
560 Hannah, W. M., Guba, O., Griffin, B. M., Feng, Y., Engwirda, D., Di Vittorio, A. V., Dang, C., Conlon, L. M., Chen, C.-C.-
561 J., Brunke, M. A., Bisht, G., Benedict, J. J., Asay-Davis, X. S., Zhang, Y., Zhang, M., Zeng, X., Xie, S., Wolfram, P. J., Vo,
562 T., Veneziani, M., Tesfa, T. K., Sreepathi, S., Salinger, A. G., Jack Reeves Eyre, J. E., Prather, M. J., Mahajan, S., Li, Q.,
563 Jones, P. W., Jacob, R. L., Huebler, G. W., Huang, X., Hillman, B. R., Harrop, B. E., Foucar, J. G., Fang, Y., Comeau, D. S.,
564 Caldwell, P. M., Bartoletti, T., Balaguru, K., Taylor, M. A., McCoy, R. B., Leung, L. R., and Bader, D. C.: The DOE E3SM
565 Model Version 2: Overview of the physical model and initial model evaluation, Journal of Advances in Modeling Earth
566 Systems, n/a, e2022MS003156, <https://doi.org/10.1029/2022MS003156>, 2022.

567 Hartmann, D. L., Ockert-Bell, M. E., and Michelsen, M. L.: The Effect of Cloud Type on Earth's Energy Balance: Global
568 Analysis, Journal of Climate, 5, 1281-1304, [https://doi.org/https://doi.org/10.1175/1520-0442\(1992\)005<1281:TEOCTO>2.0.CO;2](https://doi.org/https://doi.org/10.1175/1520-0442(1992)005<1281:TEOCTO>2.0.CO;2), 1992.

569 Hersbach, H., Bell, B., Berrisford, P., Biavati, G., Horányi, A., Muñoz Sabater, J., Nicolas, J., Peubey, C., Radu, R., Rozum,
570 I., Schepers, D., Simmons, A., Soci, C., Dee, D., and Thépaut, J.-N.: ERA5 hourly data on pressure levels from 1940 to
571 present, Copernicus Climate Change Service (C3S) Climate Data Store (CDS) [dataset],
572 <https://doi.org/10.24381/cds.bd0915c6>, 2023a. Accessed 02-March-2023.

573 Hersbach, H., Bell, B., Berrisford, P., Biavati, G., Horányi, A., Muñoz Sabater, J., Nicolas, J., Peubey, C., Radu, R., Rozum,
574 I., Schepers, D., Simmons, A., Soci, C., Dee, D., and Thépaut, J.-N.: ERA5 hourly data on single levels from 1940 to present,
575 Copernicus Climate Change Service (C3S) Climate Data Store (CDS) [dataset], <https://doi.org/10.24381/cds.adbb2d47>,
576 2023b. Accessed 02-March-2023.

577 Hersbach, H., Bell, B., Berrisford, P., Hirahara, S., Horányi, A., Muñoz-Sabater, J., Nicolas, J., Peubey, C., Radu, R.,
578 Schepers, D., Simmons, A., Soci, C., Abdalla, S., Abellan, X., Balsamo, G., Bechtold, P., Biavati, G., Bidlot, J., Bonavita,
579 M., De Chiara, G., Dahlgren, P., Dee, D., Diamantakis, M., Dragani, R., Flemming, J., Forbes, R., Fuentes, M., Geer, A.,
580 Haimberger, L., Healy, S., Hogan, R. J., Hólm, E., Janisková, M., Keeley, S., Laloyaux, P., Lopez, P., Lupu, C., Radnoti, G.,
581 de Rosnay, P., Rozum, I., Vamborg, F., Villaume, S., and Thépaut, J.-N.: The ERA5 global reanalysis, Quarterly Journal of
582 the Royal Meteorological Society, 146, 1999-2049, <https://doi.org/https://doi.org/10.1002/qj.3803>, 2020.

583 IPCC, Stocker, T. F., Qin, D., Plattner, G.-K., Tignor, M., Allen, S. K., Boschung, J., Nauels, A., Xia, Y., Bex, V., and
584 Midgley, P. M. (Eds.): Climate Change 2013: The Physical Science Basis. Contribution of Working Group I to the Fifth
585 Assessment Report of the Intergovernmental Panel on Climate Change, Cambridge University Press, Cambridge, United
586 Kingdom and New York, NY, USA, 1535 pp., <https://doi.org/10.1017/CBO9781107415324>, 2013.

587 IPCC: Climate Change 2021: The Physical Science Basis. Contribution of Working Group I to the Sixth Assessment Report
588 of the Intergovernmental Panel on Climate Change, Cambridge University Press, Cambridge, United Kingdom and New
589 York, NY, USA, 2391 pp., <https://doi.org/10.1017/9781009157896>, 2021.

590 Kirschler, S., Voigt, C., Anderson, B. E., Chen, G., Crosbie, E. C., Ferrare, R. A., Hahn, V., Hair, J. W., Kaufmann, S.,
591 Moore, R. H., Painemal, D., Robinson, C. E., Sanchez, K. J., Scarino, A. J., Shingler, T. J., Shook, M. A., Thornhill, K. L.,
592 Winstead, E. L., Ziemba, L. D., and Sorooshian, A.: Overview and statistical analysis of boundary layer clouds and



- 594 precipitation over the western North Atlantic Ocean, *Atmos. Chem. Phys.*, 23, 10731-10750, [https://doi.org/10.5194/acp-23-](https://doi.org/10.5194/acp-23-10731-2023)
595 [10731-2023](https://doi.org/10.5194/acp-23-10731-2023), 2023.
- 596 Kirschler, S., Voigt, C., Anderson, B., Campos Braga, R., Chen, G., Corral, A. F., Crosbie, E., Dadashazar, H., Ferrare, R. A.,
597 Hahn, V., Hendricks, J., Kaufmann, S., Moore, R., Pöhlker, M. L., Robinson, C., Scarino, A. J., Schollmayer, D., Shook, M.
598 A., Thornhill, K. L., Winstead, E., Ziemba, L. D., and Sorooshian, A.: Seasonal updraft speeds change cloud droplet number
599 concentrations in low-level clouds over the western North Atlantic, *Atmos. Chem. Phys.*, 22, 8299-8319,
600 <https://doi.org/10.5194/acp-22-8299-2022>, 2022.
- 601 Klein, S. A., McCoy, R. B., Morrison, H., Ackerman, A. S., Avramov, A., Boer, G. d., Chen, M., Cole, J. N. S., Del Genio,
602 A. D., Falk, M., Foster, M. J., Fridlind, A., Golaz, J.-C., Hashino, T., Harrington, J. Y., Hoose, C., Khairoutdinov, M. F.,
603 Larson, V. E., Liu, X., Luo, Y., McFarquhar, G. M., Menon, S., Neggers, R. A. J., Park, S., Poellot, M. R., Schmidt, J. M.,
604 Sednev, I., Shipway, B. J., Shupe, M. D., Spangenberg, D. A., Sud, Y. C., Turner, D. D., Veron, D. E., Salzen, K. v., Walker,
605 G. K., Wang, Z., Wolf, A. B., Xie, S., Xu, K.-M., Yang, F., and Zhang, G.: Intercomparison of model simulations of mixed-
606 phase clouds observed during the ARM Mixed-Phase Arctic Cloud Experiment. I: single-layer cloud, *Q. J. R. Meteorol. Soc.*,
607 135, 979-1002, <https://doi.org/10.1002/qj.416>, 2009.
- 608 Larson, V. E. and Golaz, J.-C.: Using Probability Density Functions to Derive Consistent Closure Relationships among
609 Higher-Order Moments, *Mon. Weather Rev.*, 133, 1023-1042, <https://doi.org/10.1175/mwr2902.1>, 2005.
- 610 Lebassi-Habtezion, B. and Caldwell, P. M.: Aerosol specification in single-column Community Atmosphere Model version
611 5, *Geosci. Model Dev.*, 8, 817-828, <https://doi.org/10.5194/gmd-8-817-2015>, 2015.
- 612 Li, X.-Y., Wang, H., Chen, J., Endo, S., Kirschler, S., Voigt, C., Crosbie, E., Ziemba, L. D., Painemal, D., Cairns, B., Hair, J.
613 W., Corral, A. F., Robinson, C., Dadashazar, H., Sorooshian, A., Chen, G., Ferrare, R. A., Kleb, M. M., Liu, H., Moore, R.,
614 Scarino, A. J., Shook, M. A., Shingler, T. J., Thornhill, K. L., Tornow, F., Xiao, H., and Zeng, X.: Large-Eddy Simulations
615 of Marine Boundary Layer Clouds Associated with Cold-Air Outbreaks during the ACTIVATE Campaign. Part II: Aerosol-
616 Meteorology-Cloud Interaction, *Journal of the Atmospheric Sciences*, 80, 1025-1045,
617 <https://doi.org/https://doi.org/10.1175/JAS-D-21-0324.1>, 2023.
- 618 Li, X.-Y., Wang, H., Chen, J., Endo, S., George, G., Cairns, B., Chellappan, S., Zeng, X., Kirschler, S., Voigt, C.,
619 Sorooshian, A., Crosbie, E., Chen, G., Ferrare, R. A., Gustafson, W. I., Hair, J. W., Kleb, M. M., Liu, H., Moore, R.,
620 Painemal, D., Robinson, C., Scarino, A. J., Shook, M., Shingler, T. J., Thornhill, K. L., Tornow, F., Xiao, H., Ziemba, L. D.,
621 and Zuidema, P.: Large-Eddy Simulations of Marine Boundary Layer Clouds Associated with Cold-Air Outbreaks during
622 the ACTIVATE Campaign. Part I: Case Setup and Sensitivities to Large-Scale Forcings, *Journal of the Atmospheric*
623 *Sciences*, 79, 73-100, <https://doi.org/10.1175/jas-d-21-0123.1>, 2022.
- 624 Lin, Y., Takano, Y., Gu, Y., Wang, Y., Zhou, S., Zhang, T., Zhu, K., Wang, J., Zhao, B., Chen, G., Zhang, D., Fu, R., and
625 Seinfeld, J.: Characterization of the aerosol vertical distributions and their impacts on warm clouds based on multi-year
626 ARM observations, *Science of The Total Environment*, 904, 166582,
627 <https://doi.org/https://doi.org/10.1016/j.scitotenv.2023.166582>, 2023.
- 628 Liu, X., Xie, S., and Ghan, S. J.: Evaluation of a new mixed-phase cloud microphysics parameterization with CAM3 single-
629 column model and M-PACE observations, *Geophys. Res. Lett.*, 34, n/a-n/a, <https://doi.org/10.1029/2007GL031446>, 2007.
- 630 Liu, X., Ma, P. L., Wang, H., Tilmes, S., Singh, B., Easter, R. C., Ghan, S. J., and Rasch, P. J.: Description and evaluation of
631 a new four-mode version of the Modal Aerosol Module (MAM4) within version 5.3 of the Community Atmosphere Model,
632 *Geosci. Model Dev.*, 9, 505-522, <https://doi.org/10.5194/gmd-9-505-2016>, 2016.
- 633 Liu, X., Xie, S., Boyle, J., Klein, S. A., Shi, X., Wang, Z., Lin, W., Ghan, S. J., Earle, M., Liu, P. S. K., and Zelenyuk, A.:
634 Testing cloud microphysics parameterizations in NCAR CAM5 with ISDAC and M-PACE observations, *J. Geophys. Res.*
635 *Atmos.*, 116, <https://doi.org/10.1029/2011jd015889>, 2011.
- 636 Liu, X., Easter, R. C., Ghan, S. J., Zaveri, R., Rasch, P., Shi, X., Lamarque, J. F., Gettelman, A., Morrison, H., Vitt, F.,
637 Conley, A., Park, S., Neale, R., Hannay, C., Ekman, A. M. L., Hess, P., Mahowald, N., Collins, W., Iacono, M. J.,
638 Bretherton, C. S., Flanner, M. G., and Mitchell, D.: Toward a minimal representation of aerosols in climate models:
639 description and evaluation in the Community Atmosphere Model CAM5, *Geosci. Model Dev.*, 5, 709-739,
640 <https://doi.org/10.5194/gmd-5-709-2012>, 2012.
- 641 Ma, P. L., Harrop, B. E., Larson, V. E., Neale, R. B., Gettelman, A., Morrison, H., Wang, H., Zhang, K., Klein, S. A.,
642 Zelinka, M. D., Zhang, Y., Qian, Y., Yoon, J. H., Jones, C. R., Huang, M., Tai, S. L., Singh, B., Bogenschutz, P. A., Zheng,
643 X., Lin, W., Quaas, J., Chepfer, H., Brunke, M. A., Zeng, X., Mülmenstädt, J., Hagos, S., Zhang, Z., Song, H., Liu, X.,



- 644 Pritchard, M. S., Wan, H., Wang, J., Tang, Q., Caldwell, P. M., Fan, J., Berg, L. K., Fast, J. D., Taylor, M. A., Golaz, J. C.,
645 Xie, S., Rasch, P. J., and Leung, L. R.: Better calibration of cloud parameterizations and subgrid effects increases the fidelity
646 of the E3SM Atmosphere Model version 1, *Geosci. Model Dev.*, 15, 2881-2916, <https://doi.org/10.5194/gmd-15-2881-2022>,
647 2022.
- 648 Minnis, P., Nguyen, L., Palikonda, R., Heck, P. W., Spangenberg, D. A., Doelling, D. R., Ayers, J. K., Smith, J. W. L.,
649 Khaiyer, M. M., Trepte, Q. Z., Avey, L. A., Chang, F.-L., Yost, C. R., Chee, T. L., and Szedung, S.-M.: Near-real time cloud
650 retrievals from operational and research meteorological satellites, *Proc. SPIE Europe Remote Sens.*, Cardiff, Wales, UK., 15-
651 18 September, 710703, <https://doi.org/10.1117/12.800344>, 2008.
- 652 Minnis, P., Sun-Mack, S., Young, D. F., Heck, P. W., Garber, D. P., Chen, Y., Spangenberg, D. A., Arduini, R. F., Trepte, Q.
653 Z., Smith, W. L., Ayers, J. K., Gibson, S. C., Miller, W. F., Hong, G., Chakrapani, V., Takano, Y., Liou, K. N., Xie, Y., and
654 Yang, P.: CERES Edition-2 Cloud Property Retrievals Using TRMM VIRS and Terra and Aqua MODIS Data—Part I:
655 Algorithms, *IEEE Transactions on Geoscience and Remote Sensing*, 49, 4374-4400,
656 <https://doi.org/10.1109/TGRS.2011.2144601>, 2011.
- 657 Painemal, D., Corral, A. F., Sorooshian, A., Brunke, M. A., Chellappan, S., Afzali Goroo, V., Ham, S.-H., O'Neill, L.,
658 Smith Jr., W. L., Tselioudis, G., Wang, H., Zeng, X., and Zuidema, P.: An Overview of Atmospheric Features Over the
659 Western North Atlantic Ocean and North American East Coast—Part 2: Circulation, Boundary Layer, and Clouds, *Journal of*
660 *Geophysical Research: Atmospheres*, 126, e2020JD033423, <https://doi.org/https://doi.org/10.1029/2020JD033423>, 2021.
- 661 Randall, D. A., Xu, K.-M., Somerville, R. J. C., and Iacobellis, S.: Single-Column Models and Cloud Ensemble Models as
662 Links between Observations and Climate Models, *J. Climate*, 9, 1683-1697, [https://doi.org/10.1175/1520-
663 0442\(1996\)009<1683:SCMACE>2.0.CO;2](https://doi.org/10.1175/1520-0442(1996)009<1683:SCMACE>2.0.CO;2), 1996.
- 664 Seethala, C., Zuidema, P., Edson, J., Brunke, M., Chen, G., Li, X. Y., Painemal, D., Robinson, C., Shingler, T., Shook, M.,
665 Sorooshian, A., Thornhill, L., Tornow, F., Wang, H., Zeng, X., and Ziemba, L.: On Assessing ERA5 and MERRA2
666 Representations of Cold-Air Outbreaks Across the Gulf Stream, *Geophys Res Lett*, 48,
667 <https://doi.org/10.1029/2021gl094364>, 2021.
- 668 Shrivastava, M., Cappa, C. D., Fan, J., Goldstein, A. H., Guenther, A. B., Jimenez, J. L., Kuang, C., Laskin, A., Martin, S. T.,
669 Ng, N. L., Petaja, T., Pierce, J. R., Rasch, P. J., Roldin, P., Seinfeld, J. H., Shilling, J., Smith, J. N., Thornton, J. A.,
670 Volkamer, R., Wang, J., Worsnop, D. R., Zaveri, R. A., Zelenyuk, A., and Zhang, Q.: Recent advances in understanding
671 secondary organic aerosol: Implications for global climate forcing, *Reviews of Geophysics*, 55, 509-559,
672 <https://doi.org/https://doi.org/10.1002/2016RG000540>, 2017.
- 673 Sorooshian, A., Corral, A. F., Braun, R. A., Cairns, B., Crosbie, E., Ferrare, R., Hair, J., Kleb, M. M., Hossein Mardi, A.,
674 Maring, H., McComiskey, A., Moore, R., Painemal, D., Scarino, A. J., Schlosser, J., Shingler, T., Shook, M., Wang, H.,
675 Zeng, X., Ziemba, L., and Zuidema, P.: Atmospheric Research Over the Western North Atlantic Ocean Region and North
676 American East Coast: A Review of Past Work and Challenges Ahead, *J. Geophys. Res. Atmos.*, 125, e2019JD031626,
677 <https://doi.org/10.1029/2019JD031626>, 2020.
- 678 Sorooshian, A., Anderson, B., Bauer, S. E., Braun, R. A., Cairns, B., Crosbie, E., Dadashazar, H., Diskin, G., Ferrare, R.,
679 Flagan, R. C., Hair, J., Hostetler, C., Jonsson, H. H., Kleb, M. M., Liu, H., MacDonald, A. B., McComiskey, A., Moore, R.,
680 Painemal, D., Russell, L. M., Seinfeld, J. H., Shook, M., Smith, W. L., Thornhill, K., Tselioudis, G., Wang, H., Zeng, X.,
681 Zhang, B., Ziemba, L., and Zuidema, P.: Aerosol–Cloud–Meteorology Interaction Airborne Field Investigations: Using
682 Lessons Learned from the U.S. West Coast in the Design of ACTIVATE off the U.S. East Coast, *Bulletin of the American*
683 *Meteorological Society*, 100, 1511-1528, <https://doi.org/https://doi.org/10.1175/BAMS-D-18-0100.1>, 2019.
- 684 Sorooshian, A., Alexandrov, M. D., Bell, A. D., Bennett, R., Betito, G., Burton, S. P., Buzanowicz, M. E., Cairns, B.,
685 Chemyakin, E. V., Chen, G., Choi, Y., Collister, B. L., Cook, A. L., Corral, A. F., Crosbie, E. C., van Dierenhoven, B.,
686 DiGangi, J. P., Diskin, G. S., Dmitrovic, S., Edwards, E.-L., Fenn, M. A., Ferrare, R. A., van Gilst, D., Hair, J. W., Harper, D.
687 B., Hilario, M. R. A., Hostetler, C. A., Jester, N., Jones, M., Kirschler, S., Kleb, M. M., Kusterer, J. M., Leavor, S., Lee, J.
688 W., Liu, H., McCauley, K., Moore, R. H., Nied, J., Notari, A., Nowak, J. B., Painemal, D., Phillips, K. E., Robinson, C. E.,
689 Scarino, A. J., Schlosser, J. S., Seaman, S. T., Seethala, C., Shingler, T. J., Shook, M. A., Sinclair, K. A., Smith Jr, W. L.,
690 Spangenberg, D. A., Starnes, S. A., Thornhill, K. L., Voigt, C., Vömel, H., Wasilewski, A. P., Wang, H., Winstead, E. L.,
691 Zeider, K., Zeng, X., Zhang, B., Ziemba, L. D., and Zuidema, P.: Spatially coordinated airborne data and complementary
692 products for aerosol, gas, cloud, and meteorological studies: the NASA ACTIVATE dataset, *Earth System Science Data*, 15,
693 3419-3472, <https://doi.org/10.5194/essd-15-3419-2023>, 2023.



- 694 Tang, S., Varble, A. C., Fast, J. D., Zhang, K., Wu, P., Dong, X., Mei, F., Pekour, M., Hardin, J. C., and Ma, P. L.: Earth
695 System Model Aerosol-Cloud Diagnostics Package (ESMAC Diags) Version 2: Assessments of Aerosols, Clouds and
696 Aerosol-Cloud Interactions Through Field Campaign and Long-Term Observations, *Geosci. Model Dev. Discuss.*, 2023, 1-
697 32, <https://doi.org/10.5194/gmd-2023-51>, 2023.
- 698 Twomey, S.: The nuclei of natural cloud formation part II: The supersaturation in natural clouds and the variation of cloud
699 droplet concentration, *Geofisica pura e applicata*, 43, 243-249, <https://doi.org/10.1007/BF01993560>, 1959.
- 700 Twomey, S.: The Influence of Pollution on the Shortwave Albedo of Clouds, *J. Atmos. Sci.*, 34, 1149-1152,
701 [https://doi.org/10.1175/1520-0469\(1977\)034<1149:TIOPOT>2.0.CO;2](https://doi.org/10.1175/1520-0469(1977)034<1149:TIOPOT>2.0.CO;2), 1977.
- 702 Varble, A. C., Ma, P. L., Christensen, M. W., Mülmenstädt, J., Tang, S., and Fast, J.: Evaluation of liquid cloud albedo
703 susceptibility in E3SM using coupled eastern North Atlantic surface and satellite retrievals, *Atmos. Chem. Phys.*, 23, 13523-
704 13553, <https://doi.org/10.5194/acp-23-13523-2023>, 2023.
- 705 Vömel, H., Sorooshian, A., Robinson, C., Shingler, T. J., Thornhill, K. L., and Ziemba, L. D.: Dropsonde observations
706 during the Aerosol Cloud meTeorology Interactions oVer the western ATLantic Experiment, *Scientific Data*, 10, 753,
707 <https://doi.org/10.1038/s41597-023-02647-5>, 2023.
- 708 Wang, H., Easter, R. C., Rasch, P. J., Wang, M., Liu, X., Ghan, S. J., Qian, Y., Yoon, J. H., Ma, P. L., and Vinoj, V.:
709 Sensitivity of remote aerosol distributions to representation of cloud–aerosol interactions in a global climate model, *Geosci.*
710 *Model Dev.*, 6, 765-782, <https://doi.org/10.5194/gmd-6-765-2013>, 2013.
- 711 Wang, H., Easter, R. C., Zhang, R., Ma, P.-L., Singh, B., Zhang, K., Ganguly, D., Rasch, P. J., Burrows, S. M., Ghan, S. J.,
712 Lou, S., Qian, Y., Yang, Y., Feng, Y., Flanner, M., Leung, R. L., Liu, X., Shrivastava, M., Sun, J., Tang, Q., Xie, S., and
713 Yoon, J.-H.: Aerosols in the E3SM Version 1: New Developments and Their Impacts on Radiative Forcing, *J. Adv. Model.*
714 *Earth Syst.*, 12, e2019MS001851, <https://doi.org/10.1029/2019ms001851>, 2020.
- 715 Warren, S. G., Hahn, C. J., London, J., Chervin, R. M., and Jenne, R. L.: Global distribution of total cloud cover and cloud
716 type amounts over the ocean, USDOE Office of Energy Research, Washington, DC (USA)
- 717 National Center for Atmospheric Research, Boulder, CO (USA), Technical Report, Report number: DOE/ER-0406, 305 pp,
718 10.2172/5415329, 1988.
- 719 Wood, R.: Stratocumulus Clouds, *Monthly Weather Review*, 140, 2373-2423, <https://doi.org/10.1175/mwr-d-11-00121.1>,
720 2012.
- 721 Xie, S., Wang, Y.-C., Lin, W., Ma, H.-Y., Tang, Q., Tang, S., Zheng, X., Golaz, J.-C., Zhang, G. J., and Zhang, M.:
722 Improved Diurnal Cycle of Precipitation in E3SM With a Revised Convective Triggering Function, *J. Adv. Model. Earth*
723 *Syst.*, 11, 2290-2310, <https://doi.org/10.1029/2019ms001702>, 2019.
- 724 Zhang, G. J. and McFarlane, N. A.: Sensitivity of climate simulations to the parameterization of cumulus convection in the
725 Canadian climate centre general circulation model, *Atmosphere-Ocean*, 33, 407-446,
726 <https://doi.org/10.1080/07055900.1995.9649539>, 1995.
- 727 Zhang, M., Deng, X., Zhu, R., Ren, Y., and Xue, H.: The Impact of Aerosol Vertical Distribution on a Deep Convective
728 Cloud, *Atmosphere*, 12, 675, 2021.

729